Supplementary information

Modulating Interfacial Ion Flux via Electrode Coatings Enables Efficient Acidic CO_2 Electrolysis

Xiaotong Li[‡,a], Xinhui Guo[‡,a,b], Qian Liu[‡,c], Yunxia He[c], Youwen Rong[a,d], Zijian Tan[a,b], Yiyuan Jiang[a], Zhou Chen[*,e], Dunfeng Gao[*,a,b], Guoxiong Wang[*,a,d], Xinhe Bao[a]

[a]State Key Laboratory of Catalysis, Dalian National Laboratory for Clean Energy, iChEM (Collaborative Innovation Center of Chemistry for Energy Materials), Dalian Institute of Chemical Physics, Chinese Academy of Sciences, Dalian 116023, China

[b]University of Chinese Academy of Sciences, Beijing 100049, China

[c]Hoffmann Institute of Advanced Materials, Shenzhen Polytechnic University, 7098 Liuxian Boulevard, Shenzhen 518055, China

[d]Department of Chemistry, Advanced Institute for Future Energy, Shanghai Key Laboratory of Electrochemical and Thermochemical Conversion for Resources Recycling, iChEM (Collaborative Innovation Center of Chemistry for Energy Materials), State Key Laboratory of Porous Materials for Separation and Conversion, Fudan University, Shanghai 200438, China

[e]College of Materials, Xiamen University, Xiamen 361005, China

[‡]These authors contributed equally: Xiaotong Li, Xinhui Guo, Qian Liu

*Corresponding authors Emails: zhouchen@xmu.edu.cn (Zhou Chen); dfgao@dicp.ac.cn (Dunfeng Gao); wanggx@dicp.ac.cn (Guoxiong Wang)

Methods

Chemicals and Materials

Carbon particles (Vulcan XC-72R, Cabot), cobalt (II) phthalocyanine (CoPc, 90.0%), aluminum oxide (Al_2O_3, 99%), and Nafion 117 dispersion (5 wt% in a mixture of lower aliphatic alcohols and water) were purchased from Macklin Corp. Potassium sulfate (K_2SO_4, 99%), sodium borohydride ($NaBH_4$, 98%), bismuth chloride ($BiCl_3$, 98%), trisodium citrate dihydrate ($Na_3C_6H_5O_7 \cdot 2H_2O$, 99%), sulfuric acid ($H_2SO_4$, 95~98%), *N, N*-dimethylformamide (DMF, 99.5%), ethanol (99.7%), and methanol (99.7%) were purchased from Sinopharm Corp. Cerium oxide (CeO_2, 99.99%) was purchased from Energy Corp. Titanium oxide (TiO_2, 99.8%, anatase phase) was obtained from Aladdin Corp. Carbon nanotubes (CNTs) was supplied by XFNANO Corp. Sustainion® XA-9 dispersion (5 wt% in ethanol) was purchased from SCI-Materials-Hub Corp, and Aquivion® D79-25BS (25 wt% in water) was obtained from Sinero Corp. Polyvinylidene fluoride (PVDF) was Solef® 5130. Polytetrafluoroethylene membrane (PTFE) with a pore size of 0.45 μm was purchased from Beijing Zhongxingweiye Instrument Company. Glass fiber was Whatman GF/D 1823. Ultrapure water (18.2 MΩ) was used in all experiments.

A 5 wt% PVDF dispersion was prepared by dissolving 0.5 g of PVDF powder in 9.5 g of DMF under continuous stirring at 300 rpm for 24 h, and was used immediately after preparation. All other chemicals were used as received without further treatment.

Catalyst synthesis and electrode preparation

1. Synthesis of Bi/C nanoparticles

The Bi/C nanoparticles were synthesized via a chemical reduction method. Briefly, 0.5 mmol of bismuth chloride ($BiCl_3$) and 8 mmol of trisodium citrate dihydrate ($Na_3C_6H_5O_7 \cdot 2H_2O$) were dissolved in 200 mL of deionized water, followed by the addition of 0.2 g of carbon nanoparticles (Vulcan XC-72R). After sonication for 2 h, a sodium borohydride solution (30 mmol of $NaBH_4$ in 300 mL of ethanol) was added, and the mixture was stirred at 500 rpm for 30 min. The Bi/C nanoparticles were collected by centrifugation, washed three times each with deionized water and ethanol, and dried in a vacuum oven at 60 °C for 24 h.

2. Preparation of Cu electrode

A hydrophobic PTFE membrane with a pore size of 0.45 μm was used directly as the substrate. The Cu electrode was fabricated using a magnetron sputtering system equipped with a high-purity Cu target (99.999%). The sputtering parameters were set as follows: power, 100 W; Ar flow rate, 37 mL min^{-1}; pressure, 6.1 mTorr; sputtering rate, 16 nm min^{-1}; and sputtering time, 25 min.

3. Preparation of a coating-modified Cu electrode

A drop-casting method was used to fabricate coating-modified Cu electrodes. First, a filler-binder composite slurry was prepared by sonication. This slurry was then drop-casted onto the Cu film and dried on a hot plate at 80 °C in a fume hood. Detailed preparation procedures for each type of coated Cu electrode were described in detail below.

For the carbon-binder composite-coated Cu electrode, 8 mg of carbon (Vulcan XC-72R or carbon nanotubes) and 40 mg of Nafion 117 dispersion (5 wt%), 40 mg of Sustainion® XA-9 dispersion (5 wt%), or 8 mg of Aquivion® D79-25BS dispersion (25 wt%) were dispersed in 10 mL of methanol and sonicated for 1 h to obtain a homogeneous slurry. When PVDF (5 wt%) was employed as the binder, DMF served as the dispersing solvent. The binder content in the slurry was fixed at 20 wt%, unless otherwise noted. The resulting coated Cu electrodes were denoted as C/CEI-Cu (Nafion 117 as binder), C/CEI_{Low}-Cu (Aquivion® D79-25BS as binder), C/AEI-Cu (Sustainion® XA-9 as the binder), C/NI-Cu (PVDF as the binder), and CNTs/CEI-Cu (CNTs as filler and Nafion 117 as binder). Moreover, 20 mg and 60 mg of Nafion 117 dispersion, corresponding to 11 wt% and 27 wt% Nafion 117 content in the slurry, respectively, were also mixed with 8 mg of carbon nanoparticles, yielding the C/$CEI_{11wt\%}$-Cu and C/$CEI_{27wt\%}$-Cu electrodes. ~2.3 μm-thick and ~5 μm-thick coatings corresponded to the C/CEI loading of 0.4 and 0.8 mg cm^{-2}, respectively.

For the oxide-CEI composite-coated Cu electrodes, 10 mg of metal oxides (Al_2O_3, CeO_2, and TiO_2) and 40 mg of Nafion 117 dispersion were dispersed in 4 mL of ethanol and sonicated for 1 h to form a homogeneous slurry. The resulting electrodes were denoted as Al_2O_3/CEI-Cu, CeO_2/CEI-Cu, and TiO_2/CEI-Cu. Moreover, Al_2O_3/CEI_{Low}-Cu, Al_2O_3/NI-Cu, and Al_2O_3/AEI-Cu electrodes were prepared by replacing the Nafion 117 dispersion in the composite slurry with Aquivion® D79-25BS, PVDF, and Sustainion® XA-9 dispersions, respectively.

For the CEI-coated Cu electrode, 10 mg of Nafion 117 dispersion was diluted in 2 mL of ethanol and drop-casted directly onto the Cu film. The resulting electrode was denoted as CEI-Cu.

4. Preparation of coating-modified CoPc and Bi electrode

For the coating-modified CoPc electrode, a CoPc catalyst layer was first prepared by drop-casting a slurry containing 1.9 mg of CoPc, 7.7 mg of XC-72R, and 19.3 mg of Nafion 117 dispersion in 5 mL of ethanol onto a gas diffusion electrode (GDE, YLS-30T, 2.2 × 2.2 cm^2), followed by drying on a hot plate at 80 °C. An Al_2O_3/CEI coating was subsequently deposited on the CoPc catalyst layer. The resulting electrode was denoted as Al_2O_3/CEI-CoPc.

For the coating-modified Bi electrode, a Bi catalyst layer was first fabricated by drop-casting a slurry containing 10 mg of Bi/C nanoparticles and 22.2 mg of Nafion 117 dispersion in 5 mL of ethanol onto a GDE and drying on a hot plate at 80 °C. An Al_2O_3/CEI coating was then deposited on the Bi catalyst layer. The resulting electrode was denoted as Al_2O_3/CEI-Bi.

Material characterization

The morphologies of samples were characterized using a field-emission scanning electron microscope (SEM, JSM-7900F), equipped with an energy-dispersive X-ray spectroscopy (EDS) system. Water contact angles were measured with a drop shape analyzer (DSA100). Cross-sectional specimens were prepared and imaged using a focused ion beam-scanning electron microscope (FIB-SEM, Helios 5CX) equipped with an EDS

system, with the sample stage tilted at 52°. Powder X-ray diffraction (XRD) patterns of the catalysts were recorded with a PANalytical X'pert PPR diffractometer with a Cu Kα radiation source (λ=1.5418 Å) at 40 kV and 40 mA at a scan rate of 10° min^{-1}. X-ray photoelectron spectroscopy (XPS) and Auger electron spectroscopy (AES) measurements were performed on an ESCALab 250Xi+ system (Thermo Fisher Scientific).

Evaluation of acidic CO_2 electrolysis performance

Acidic CO_2 electrolysis was performed in a flow cell consisting of a graphite flow-field plate, a catholyte chamber, an anolyte chamber, and a titanium backplate. The electrolysis was carried out in chronopotentiometry mode using an Autolab PGSTAT302N workstation equipped with a current booster (10 A), operating in a three-electrode configuration. Ir black deposited on Ti foam, an Ag/AgCl, and the as-prepared electrode were used as the counter, reference, and working electrodes, respectively. The catholyte and anolyte chambers were separated by a Nafion 211 membrane. A CO_2 gas stream containing 5% N_2 (as an internal standard) was continuously fed to the back side of the cathode at a flow rate of 20 mL min^{-1}, controlled by a mass flow controller (MFC), unless otherwise noted. Freshly prepared 0.5 M K_2SO_4 (adjusted to pH 2 with H_2SO_4) and 0.2 M H_2SO_4 were continuously supplied to the catholyte and anolyte chambers, respectively, unless otherwise stated. The electrolyte flow rate was maintained at 5 mL min^{-1} using a peristaltic pump in a non-recirculating mode.

To evaluate the energy efficiency, full-cell measurements were carried out in a slim flow cell equipped with a graphite flow-field plate, a 1.2 mm-thick catholyte chamber, and a titanium flow-field plate for anolyte supply. A two-electrode configuration was adopted. All other operating conditions were identical to those used in the aforementioned flow cell.

The gaseous and liquid products from CO_2 electrolysis were quantified using online gas chromatography (GC) and ^1H nuclear magnetic resonance spectroscopy (^1H NMR), respectively. The Faradaic efficiency (FE) of electrolysis products was calculated according to Equation (1). The single-pass CO_2 conversion efficiency (SPCE) was determined using Equation (2). The full-cell energy efficiency (EE) for acidic CO_2 electrolysis was calculated according to Equation (3). The working potentials were converted to the reversible hydrogen electrode (RHE) scale with an 85 % *iR* compensation, as shown in Equation (4).

$$\mathrm{FE} = \frac{\mathrm{z} \times \mathrm{F} \times n}{Q} \quad (1)$$

where z is the electron transfer for a specific product molecule, F is the Faraday's constant (96485 C mol^{-1}), n is the amount of product (in mol), and Q is the total charge passed (in C).

$$\mathrm{SPCE}\ (\%) = \frac{j_{\mathrm{products}} \times 60 \times t}{z \times \mathrm{F}} \times \frac{V_{\mathrm{m}}}{\upsilon \times t} \quad (2)$$

where $j_{products}$ is the partial current of a specific product (in A), t is the running time (in min), V_m is the molar volume (= 24500 mL mol^{-1}), and υ is the flow rate of CO_2 (in mL min^{-1}). The SPCE for C_{2+} products was calculated as the sum of the SPCEs of all individual C_{2+} products.

$$\mathrm{EE}\ (\%) = \frac{E^{n}_{product} \times FE_{product}}{E_{cell}} (3)$$

where $E^{n}_{product}$ is the thermoneutral voltage for the formation of a specific product, E_{cell} is the full-cell voltage (without Ohmic loss correction), and $FE_{product}$ is the calculated FE for the corresponding product. The EE for total CO_2 electrolysis products or for C_{2+} products was calculated as the sum of the EE values of the respective products.

$$E\ (\mathrm{vs\ RHE}) = E\ (\mathrm{vs\ Ag/AgCl}) + 0.198 + 0.059 \times \mathrm{pH} - 0.85 \times iR \quad (4)$$

where *i* is the current (in A) and *R* is the solution resistance (in Ω).

HER polarization behavior measurement

The hydrogen evolution reaction (HER) polarization behavior of the electrode was evaluated by linear sweep voltammetry (LSV) in an H-cell separated by a Nafion 117 membrane. The catholyte and anolyte chambers were filled with Ar-saturated 0.5 M K_2SO_4 (pH 2) and 0.2 M H_2SO_4, respectively. The electrode (geometric area: 1 cm^2), Ag/AgCl, and Pt wire electrode served as the working, reference, and counter electrodes, respectively. During the measurements, the catholyte was stirred at 300 rpm using a magnetic stirrer. LSV tests were conducted over a potential range of –0.1 V to –2.0 V vs RHE at a scan rate of 10 mV s^{-1}. The potential was converted to the RHE scale without *iR* compensation.

K^+ adsorption measurement

An electrode (geometric area: 1 cm^2) was first immersed in 0.5 M K_2SO_4 (pH 2) and polarized at a constant potential of –1.2 V vs RHE for 60 s, followed by transferring it into 10 mL of deionized water and shaking for 10 s. This process was repeated 5 times to collect the K^+ ions adsorbed on the electrode surface. During each transfer, the applied potential was maintained. An electrode without a potential application served as the blank control. The K^+ concentration in the collected deionized water was quantified using ion chromatography (DIONEX ICS-5000, Thermo Fisher Scientific). The adsorbed-K^+ concentration for each electrode was determined by subtracting the K^+ concentration measured under the blank condition from that obtained under polarization.

Ion-exchange properties measurement

A carbon-binder composite slurry was spray-coated on both sides of a glass fiber (GF-D) substrate to prepare the separator. The separator was then placed in the middle of an H-cell. In one chamber, 30 mL of 0.05 M H_2SO_4 or 1 M KOH aqueous solution was used as the donor solution, while the other chamber was filled with 30 mL of deionized water or 0.5 mM KOH as the receiver solution, respectively. The pH evolution of the receiver solution was monitored over time using a pH meter, providing insights into the H^+ or OH^- exchange ability of different binders.

Rotating disk electrode (RDE) measurement

RDE measurements were carried out using a DEINTYCO rotator (RRDE-1A) in an Ar-saturated 0.5 M K_2SO_4 electrolyte (pH 2). Before each measurement, the Cu disk

electrode (5 mm in diameter) was sequentially sonicated in 0.1 M HNO_3, deionized water, acetone, and deionized water for 2 min each, followed by mechanical polishing with 50 nm alumina polishing powder and a final sonication in deionized water for 3 min. To prepare the modified Cu disk electrodes, 20 mg of oxide (Al_2O_3, CeO_2, or TiO_2) and 220 mg of Nafion 117 dispersion were dispersed in 2 mL of ethanol and sonicated for 1 h. Then, 20 μL of the resulting slurry was drop-casted onto the Cu disk electrode and dried under infrared light. During measurements, an Ag/AgCl electrode and a Pt wire were used as reference and counter electrodes, respectively. Cyclic voltammetry (CV) tests were recorded over a potential range of –0.1 V to –2.5 V vs RHE at a scan rate of 50 mV s^{-1} and rotation rates of 400, 800, 1200, 1600, and 2400 rpm.

The effective proton diffusion coefficient ($D_{H+,\,eff}$) can be inferred from the slope of the linear fit between the proton mass-transfer-limited plateau current density ($|j_{plateau}|$) and the square root of rotation rate ($\omega^{1/2}$), using the Levich equation (Equation 5). In this work, this slope was used as a quantitative indicator of $D_{H+,\,eff}$.

$$j_{plateau} = 0.62 \times n \times F \times A \times D^{\frac{2}{3}} \times \upsilon^{-\frac{1}{6}} \times c \times \omega^{\frac{1}{2}} \quad (5)$$

where n is the number of electrons transferred in the reaction, F is the Faraday's constant, A is the electrode surface area, D is the proton diffusion coefficient, υ is the kinematic viscosity of the electrolyte, c is the proton concentration, and ω is the angular rotation rate.

The decrease in the $D_{H+,\,eff}$ for the modified Cu RDE was quantified using Equation (6).

$$\frac{D_{modified\ Cu\ RDE}}{D_{Cu\ RDE}} = \left(\frac{slope_{modified\ Cu\ RDE}}{slope_{Cu\ RDE}}\right)^{\frac{3}{2}} \quad (6)$$

Quasi-*in situ* XPS measurement

The Cu and Al_2O_3/CEI-Cu electrodes were electrolyzed for 30 min at 400 mA cm^{-2} under acidic CO_2 electrolysis conditions in a glovebox and subsequently transferred into a sealed XPS UHV chamber for XPS and AES measurements.

***In situ* X-ray absorption spectroscopy measurement**

X-ray absorption (XAS) spectroscopy was carried out using the *RapidXAFS* 2M (Anhui Absorption Spectroscopy Analysis Instrument Co., Ltd.) by transmission mode at 20 kV and 20 mA, and the Si (553) spherically bent crystal analyzer with a radius of curvature of 500 mm was used for Cu. The energy was calibrated to the absorption edge of a Cu foil (8979 eV). *In situ* XAS was carried out in a three-electrode system on the electrochemical workstation (CHI760E) with CO_2-saturated 0.5 M K_2SO_4 (pH 2) as the catholyte. Potentiostatic electrolysis was carried out at –1.02 V and –2.02 V vs Ag/AgCl. Every spectrum was recorded after 2 min of continuous CO_2 electrolysis.

***In situ* Raman spectroscopy measurement**

In situ Raman spectroscopy was carried out using an inVia Reflex Raman microscope (Renishaw) equipped with a 785 nm diode laser and a 50 × water immersion objective in a commercial Raman flow cell (C031-3, Gaoss Union). The spectrometer was first calibrated

using the characteristic Raman band of a silicon wafer. Each spectrum was then collected in static mode with 1% laser power and an exposure time of 60 s.

During electrochemical testing, 0.5 M K_2SO_4 (pH 1) and 0.2 M H_2SO_4 were continuously supplied to catholyte and anolyte chambers, respectively, at a flow rate of 20 mL min^{-1}. CO_2 gas was continuously fed to the backside of the cathode at a flow rate of 10 mL min^{-1}. The CO_2 electrolysis was carried out in a chronoamperometry mode on an Ivium workstation using a three-electrode configuration, with an Ag/AgCl electrode and a carbon rod serving as reference and counter electrodes, respectively. The applied potential ranged from –0.67 V to –0.92 V vs Ag/AgCl with a potential interval of –0.05 V.

To determine the local pH, a calibration curve was established by correlating the logarithm of the Gaussian-fitted Raman peak area ratio of CO_3^{2-} to HCO_3^- with the bulk pH. Calibration solutions were prepared by dissolving K_2CO_3 and $KHCO_3$ at various concentration ratios, maintaining a total K^+ concentration of 1 M.

In situ attenuated total reflectance surface-enhanced infrared absorption spectroscopy measurement

In situ ATR-SEIRAS measurement was conducted using an INVENIO S FTIR spectrometer with an MCT detector. A home-made H-cell was used for ATR-SEIRAS measurement, with a Pt wire as a counter electrode and an Ag/AgCl electrode as a reference electrode. The catholyte was CO_2-saturated 0.5 M K_2SO_4 (pH 1), and the anolyte was 0.2 M H_2SO_4. For the working electrode, an Au film was sputtered onto a silicon prism, followed by drop-casting a catalyst ink onto the Au film. All spectra were recorded as a relative change in absorbance, referenced to background spectra collected at open-circuit potential (OCP).

COMSOL Multiphysics simulation

A one-dimensional domain was constructed in COMSOL Multiphysics 6.0 to simulate local species concentrations in the vicinity of electrodes (**Scheme S1**). The computational domain comprised three sequential regions: the catalyst layer, the filler layer, and the diffusion layer. Mass transport was described using the steady-state Nernst-Planck equations coupled with the electroneutrality condition:

$$\nabla j_i = R_i \quad (7)$$

$$j_i = -D_i \nabla c_i - z_i u_{m,i} F c_i \nabla V \quad (8)$$

$$\sum_i z_i c_i = 0 \quad (9)$$

$$i = \mathrm{CO_2},\ \mathrm{HCO_3^-},\ \mathrm{CO_3^{2-}},\ \mathrm{H^+},\ \mathrm{OH^-},\ \mathrm{K^+},\ \mathrm{SO_4^{2-}}$$

where j_i is the flux of species i. R_i is the reaction term, accounting for contributions from charge-transfer reactions and carbonate equilibria. The operator ∇ stands for the spatial derivative (d/dx). c_i is the concentration of species i in solution, while D_i, z_i, and u_i correspond to its diffusivity, charge number, and ion mobility, respectively. F is the Faraday constant. The V represents the potential.

In the catalyst layer and filler layer, the diffusion coefficients were corrected for porosity. The effective diffusion coefficients were calculated using the Bruggeman relation:

$$D_{i,eff} = \frac{\varepsilon_p}{\tau_p} D_{F,i} \quad (10)$$

$$\tau_p = \varepsilon_p{}^{-1/2} \quad (11)$$

where $D_{F,i}$ is the bulk diffusion coefficient of species i, ε_p is porosity (assumed to be 0.7), and τ_p is the tortuosity. For coated Cu electrodes with a low-$D_{H+,\,eff}$ coating, the diffusion coefficients in the filler layer were further reduced by a factor of 0.1.

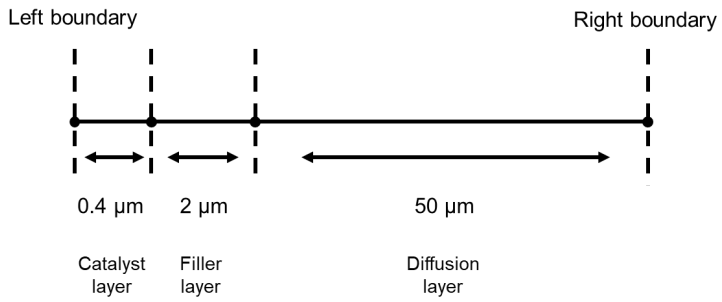

Scheme S1. The modelling geometry of the coated Cu electrode.

The hydrogen evolution reaction (HER) and acidic CO_2 electrolysis take place in the catalyst layer, where CO_2 is consumed and OH^- is generated. The FEs were assumed to be 15 % for H_2, 20 % for CO, 5 % for CH_4, 5 % for HCOOH, 30 % for C_2H_4, 10 % for C_2H_5OH, 10 % for CH_3OOH, and 5 % for C_3H_7OH.

Homogeneous reactions were presented in all domains. The reversible reactions among H^+, OH^-, CO_2, HCO_3^-, and CO_3^{2-} included in the model were:

$$CO_2(aq) + H_2O \overset{k_1,k_{-1}}{\longleftrightarrow} H^+ + HCO_3^- \qquad K_1$$

$$HCO_3^- \overset{k_2,k_{-2}}{\longleftrightarrow} H^+ + CO_3^{2-} \qquad K_2$$

$$CO_2(aq) + OH^- \overset{k_3,k_{-3}}{\longleftrightarrow} HCO_3^- \qquad K_3$$

$$HCO_3^- + OH^- \overset{k_4,k_{-4}}{\longleftrightarrow} H_2O + CO_3^{2-} \qquad K_4$$

At the left boundary, a constant CO_2 concentration was imposed, while zero-flux conditions were applied to all other aqueous species. The aqueous CO_2 concentration ($[CO_2]_{aq}$) was calculated from the gas-phase pressure, temperature, and solution salinity using Henry's law and the Séchenov equation[1]. At the right boundary, equilibrium concentration values corresponding to the bulk electrolyte were imposed.

Henry's law is given by:

$$[CO_2]_{aq,\ H} = K_H[CO_2]_g \ (12)$$

$$K_H = 93.4517\left(\frac{100}{T}\right) - 60.2409 + 23.3585\left(\frac{100}{T}\right) \ (13)$$

where K_H is Henry's constant (34.1 mM atm^{-1} at T = 298.15 K). T is the temperature of the solution in K.

The Séchenov equation is expressed as:

$$log\left(\frac{[CO_2]_{aq,H}}{[CO_2]_g}\right) = K_s[C_s] \ (14)$$

where K_s is the Séchenov constant and $[C_s]$ is the molar concentration of the electrolyte.

$$K_s = \sum (h_{ion} - h_G) \ (15)$$

$$h_G = h_{G,o} + h_T(T - 298.15) \ (16)$$

h_{ion}, $h_{g,o}$, and h_T is ion-specific parameter, gas-specific parameter, and gas-specific parameter, respectively.

Table S1. Diffusion coefficient in bulk solution.

Ion	Diffusion coefficient (10^{-9} m^2 s^{-1})
H^+	9.310
K^+	1.957
OH^-	5.273
SO_4^{2-}	1.065
CO_3^{2-}	0.923
HCO_3^-	1.185
CO_2	1.910

Table S2. The homogeneous reaction parameters.

Parameter	Explanation	Value	Unit	Reference
K_1	Equilibrium constant	4.27×10^{-7}	mol L^{-1}	2
K_2	Equilibrium constant	4.59×10^{-11}	mol L^{-1}	2
K_3	Equilibrium constant	K_1/K_w	mol^{-1} L s^{-1}	2
K_4	Equilibrium constant	K_4/K_w	mol^{-1} L	2

K_w	Dissociation constant of water	10^{-14}	$mol^{-2}\ L^2$	3
k_{w1}	Rate constant of water dissociation	10^{-3}	$mol\ L^{-1}\ s^{-1}$	4
k_1	Rate constant	3.71×10^{-2}	s^{-1}	4
k_2	Rate constant	59.44	s^{-1}	4
k_3	Rate constant	2.23×10^3	$mol^{-1}\ L\ s^{-1}$	4
k_4	Rate constant	6×10^9	$mol^{-1}\ L\ s^{-1}$	4

Table S3. Séchenov constants.

Ion	**h_{ion}**
K^+	0.0922
SO_4^{2-}	0.1117
CO_3^{2-}	0.1423
OH^-	0.0839
HCO_3^-	0.0967
Other parameters	
$h_{G,0}$	−0.0172
h_T	−0.000338

Theoretical calculation

Density functional theory (DFT) calculations were performed by using the Vienna ab initio simulation package (VASP)[5, 6] with a plane-wave basis set and an energy cutoff of 500 eV. The projector augmented wave (PAW) potential was employed to describe the electron-ion interactions.[7] The generalized gradient approximation with the Perdew-Burke-Ernzerhof (GGA-PBE) functional was applied to treat the exchange-correlation energy.[8, 9] Grimme's semiempirical DFT-D3 dispersion correction was adopted to account for the van der Waals (vdW) interactions.[10] The convergence criteria of the residual Hellmann-Feynman force and total energy during structure optimization were set to 0.02 eV $Å^{-1}$ and 10^{-5} eV, respectively. The Al_2O_3 (116), CeO_2 (311), and TiO_2 (211) crystal planes were cleaved, and all slab models were modeled with a vacuum layer of 20 Å.

To determine the energy barriers for proton transport and accurately identify the corresponding transition state (TS) structures, the climbing-image nudged elastic band (CI-NEB) method was employed.[11] All atomic positions were fully relaxed during the NEB calculations. After geometry optimization, single-point energy recalculations were performed

for all configurations to correct for systematic errors associated with changes in the plane-wave basis set during structural relaxation, thereby ensuring reliable energy evaluations.

The *ab initio* molecular dynamics (AIMD) simulations were carried out using the Quickstep module with the CP2K package, which enables efficient computations in systems containing plentiful explicit water molecules.[12] The core electrons of Cu, K, H, O, and C atoms were described by the Goedecker-Teter-Hutter (GTH)-type pseudopotentials[13, 14], while their valence orbitals were expanded using Gaussian and auxiliary plane-wave (GPW)-type double-ζ basis sets[15] with one set of polarization functions (DZVP)[16]. A plane-wave cutoff of 300 Ry was used for density expansion. The PBE functional[9] was used to describe electron exchange and correlation energies, with Grimme D3 dispersion corrections[10]. During the AIMD simulations, the self-consistent field convergence criterion was set to 10^{-5} Ry for both electronic gradients and total energies, with a timestep of 1 fs. The simulations were run for 2000 fs under a canonical ensemble (NVT), with the temperature maintained at 298.15 K using CSVR thermostats[17]. The supercell size is 13.28 × 10.22 × 43.45 Å3, filled with multiple explicit water layers (ca. 50 H_2O) at a density of ~1.0 g cm^{-3}, and a 15 Å vacuum region was included to prohibit spurious periodic interactions. Input files for CP2K calculations were generated using the Multiwfn software.[18, 19]

The adsorption energy (E_{ads}) was calculated as follows:

$$E_{ads} = E_{adsorbate+slab} - E_{slab} - E_{adsorbate} \quad (17)$$

where $E_{adsorbate+slab}$, E_{slab}, and $E_{adsorbate}$ are the total energies of the slab with adsorbates, clean slab, and the isolated adsorbate, respectively.

The Gibbs free energy diagrams were calculated following the approach developed by Nørskov et al.,[20] in which the ΔG is evaluated as:

$$\Delta G = \Delta E + \Delta ZPE - T\Delta S + \Delta G_U + \Delta G_{pH} + \Delta G_{field} \quad (18)$$

where ΔE, ΔZPE, and Δ*S* are the reaction energy, the zero-point energy correction, and entropy change, respectively. *T* is the temperature (set to 298.15 K). $\Delta G_U = eU$ is the free energy contribution related to electrode potential *U*. ΔG_{pH} is the correction of the H^+ free energy, which can be calculated through $\Delta G_{pH} = k_B T \times \ln 10 \times pH$. The k_B is the Boltzmann constant, and pH is set to 0 (acidic medium). ΔG_{field} is the free-energy correction from the electric double layer, which is negligible in this study.

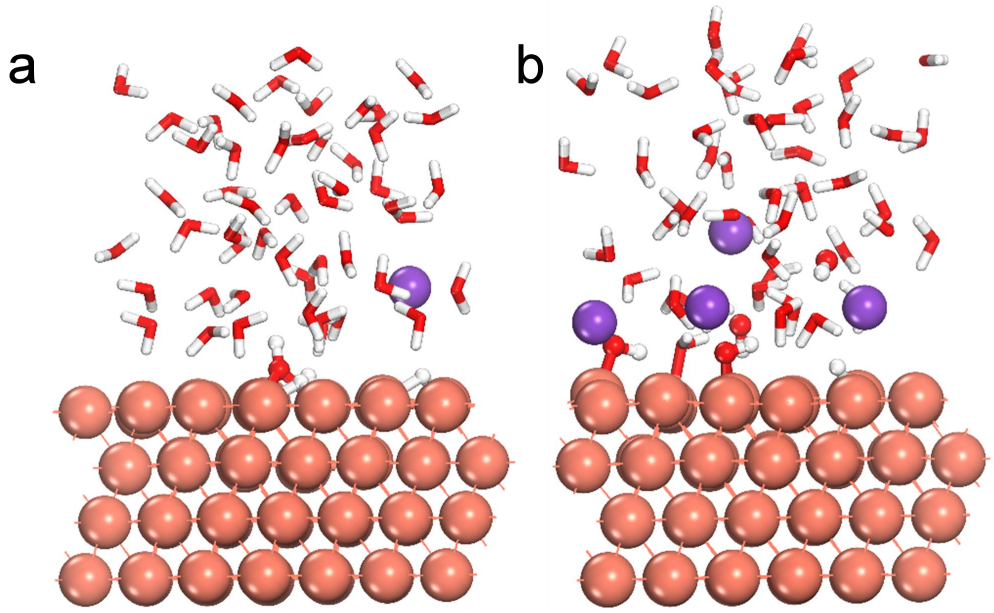

Fig. S1. Optimized configurations used in AIMD simulations. Cu (111) surface with (a) one K-OH pair and three H atoms, and (b) four K-OH pairs and one H atom.

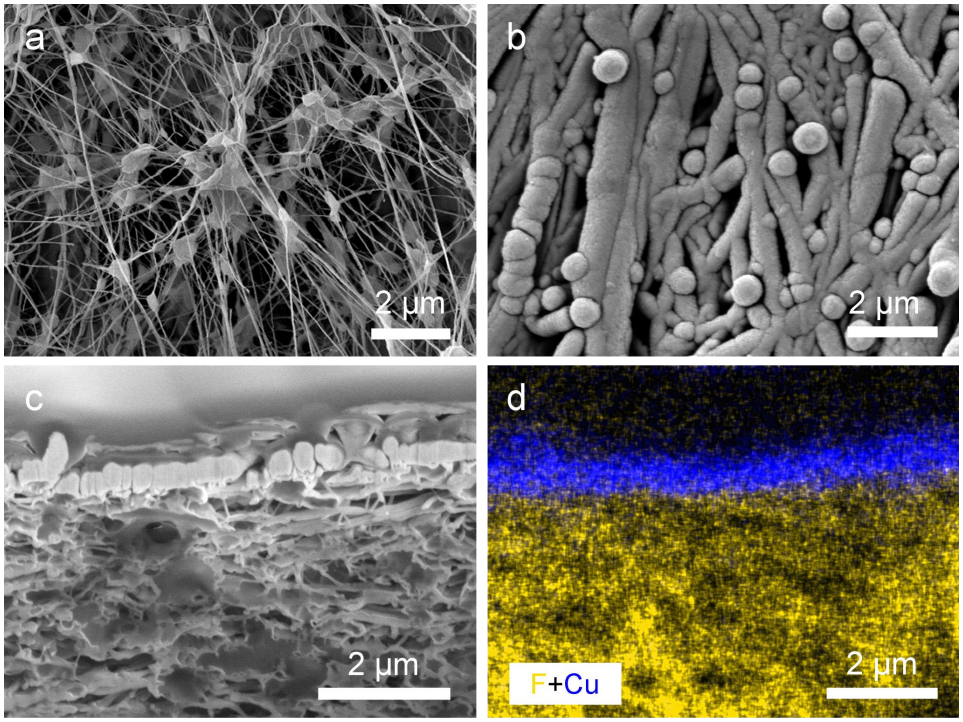

Fig. S2. (a-b) SEM images of (a) pristine PTFE membrane and (b) Cu electrode. (c) Focused ion beam (FIB)-milled cross-sectional SEM image acquired at a 52° sample tilt and (d) corresponding EDS elemental maps of the Cu electrode.

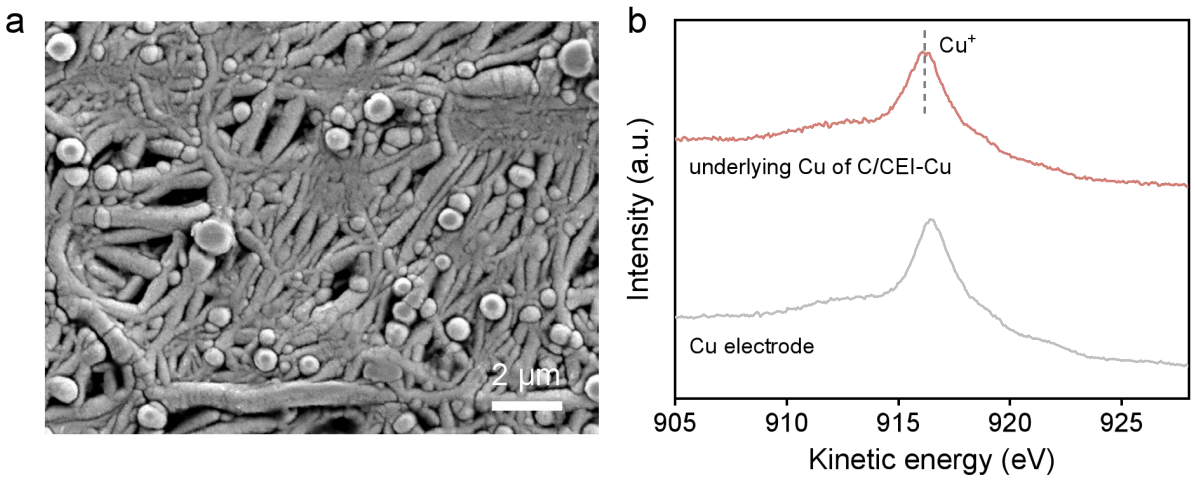

Fig. S3. (a) SEM image of the underlying Cu of the C/CEI-Cu electrode. (b) Cu LMM AES spectra of the Cu electrode and the underlying Cu of the C/CEI-Cu electrode.

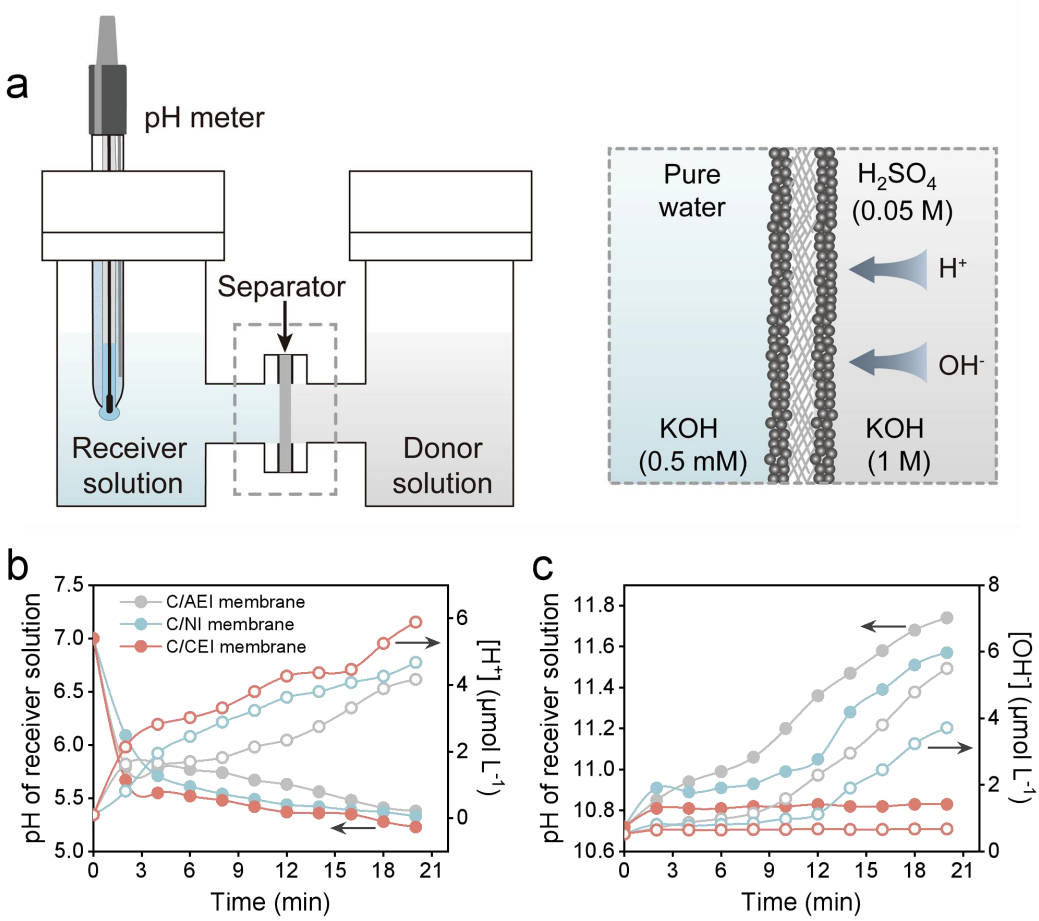

Fig. S4. (a) Schematic illustration of the H-cell for ion-exchange properties measurement. (b, c) Time-dependent pH variation in the receiver solution during (b) H^+-exchange and (c) OH^--exchange measurements using different membranes.

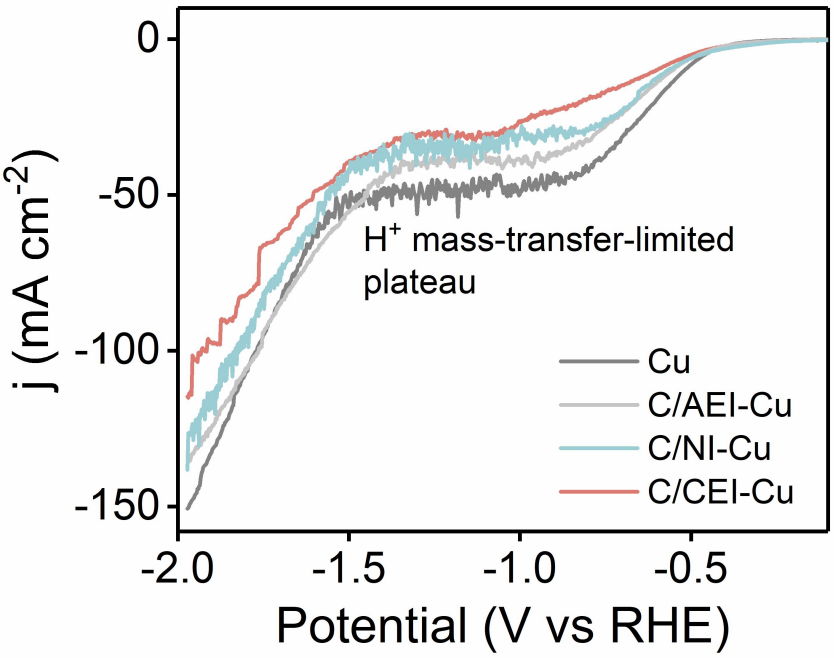

Fig. S5. HER polarization curves of Cu and coated Cu electrodes in an H-cell.

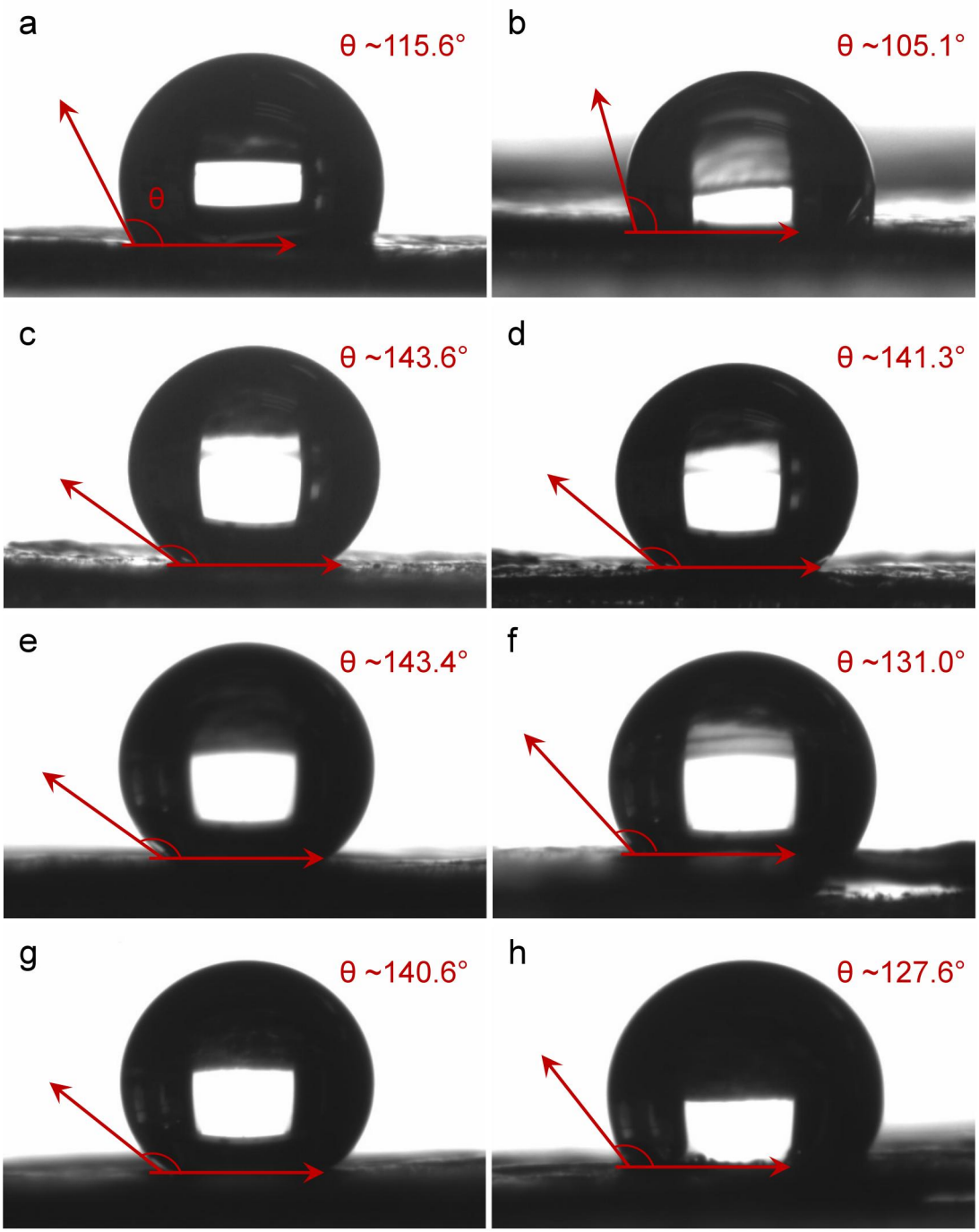

Fig. S6. Contact angles of (a, b) Cu, (c, d) C/CEI-Cu, (e, f) C/NI-Cu, and (g, h) C/AEI-Cu electrodes (a, c, e, g) before and (b, d, f, h) after acidic CO_2 electrolysis at 300 mA cm^{-2} for 0.5 h in 0.5 M K_2SO_4 (pH 2).

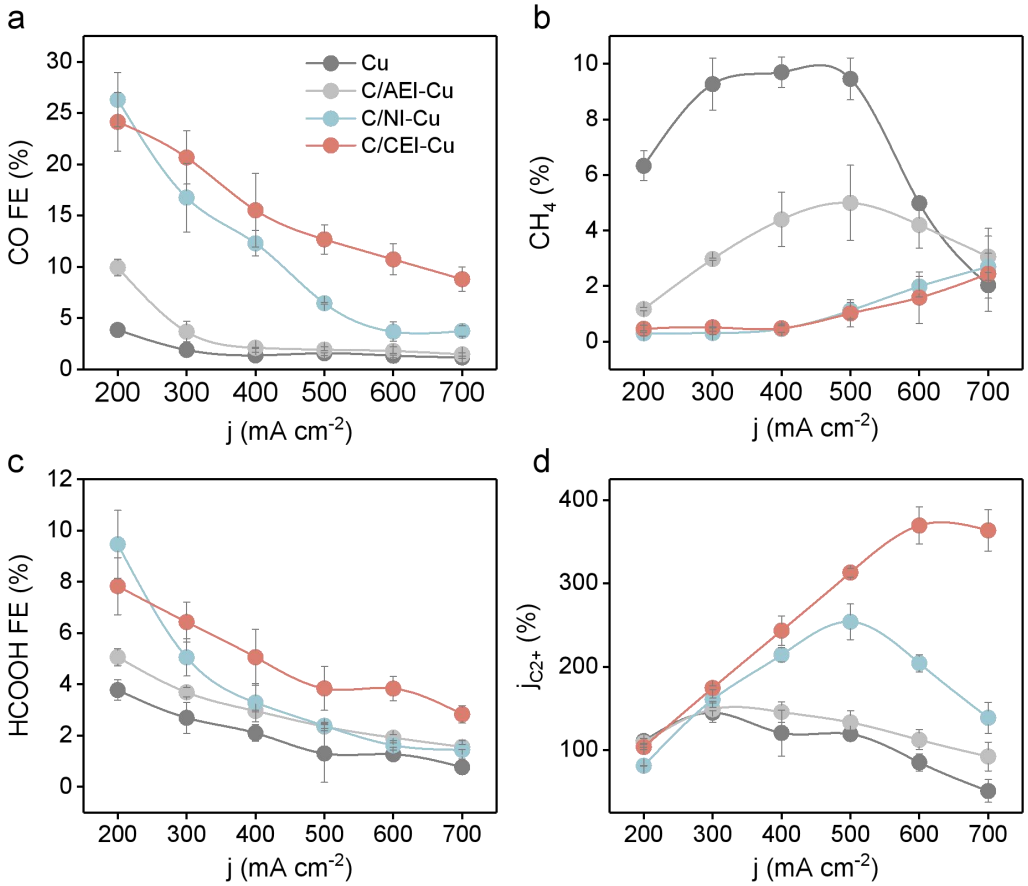

Fig. S7. (a-c) FEs of (a) CO, (b) CH_4, (c) HCOOH, and (d) partial current density of C_{2+} products (j_{C2+}) as a function of current density on Cu, C/AEI-Cu, C/NI-Cu, and C/CEI-Cu electrodes in 0.5 M K_2SO_4 (pH 2).

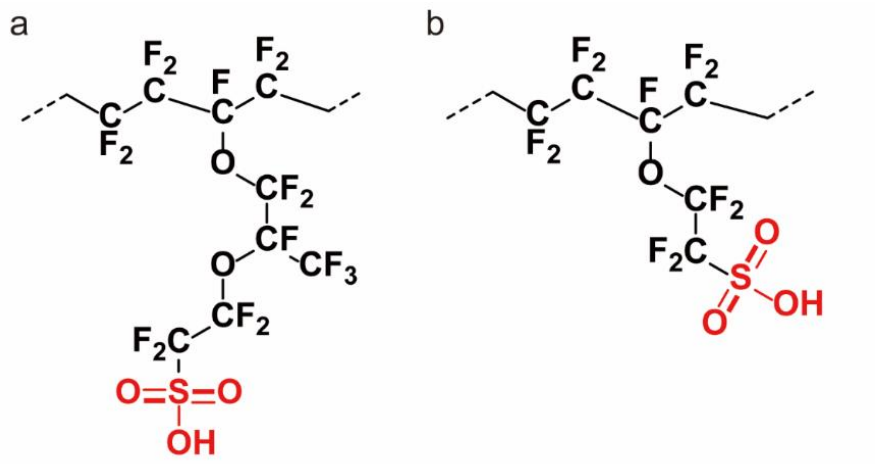

Fig. S8. Chemical structure of (a) Nafion 117 (equivalent weight, EW = 1100 g mol^{-1} SO_3H) and (b) Aquivion D79-25BS (EW = 790 g mol^{-1} SO_3H). The ion exchange capacity (IEC) is inversely proportional to the EW of the CEI, with a higher IEC corresponding to a lower EW.

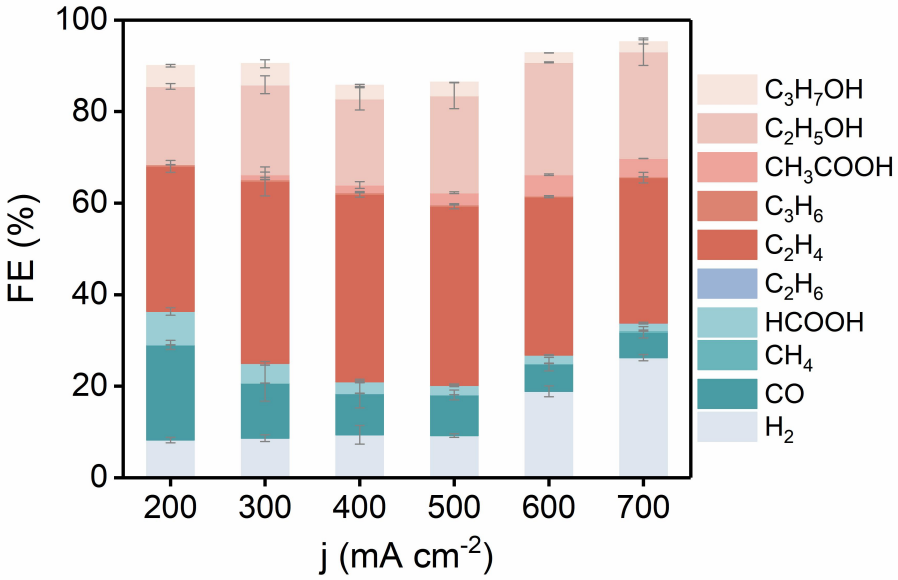

Fig. S9. Product distributions for acidic CO_2 electrolysis on the C/CEI$_{Low}$-Cu electrode in 0.5 M K_2SO_4 (pH 2).

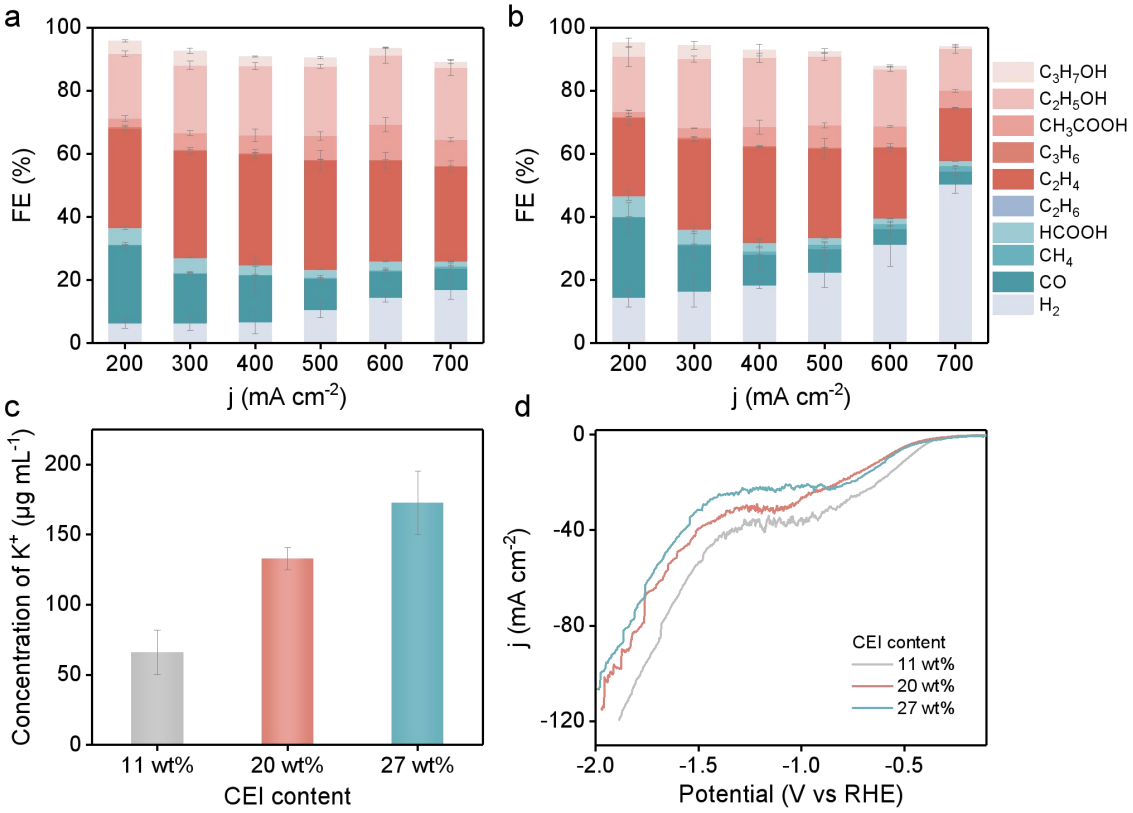

Fig. S10. (a-b) Product distributions for acidic CO_2 electrolysis on (a) C/CEI$_{27wt\%}$-Cu and (b) C/CEI$_{11wt\%}$-Cu electrodes in 0.5 M K_2SO_4 (pH 2). (c) Adsorbed-K^+ concentrations on C/CEI-coated Cu electrodes with varying CEI contents. (d) HER polarization curves of C/CEI-coated Cu electrodes with varying CEI contents.

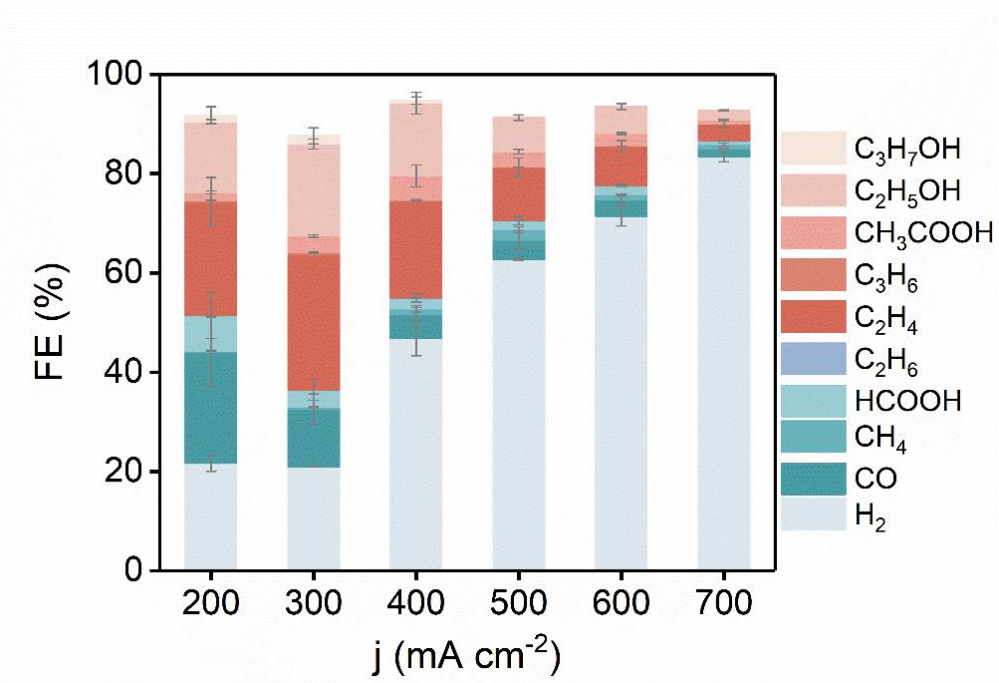

Fig. S11. Product distributions for acidic CO_2 electrolysis on the CEI-Cu electrode in 0.5 M K_2SO_4 (pH 2).

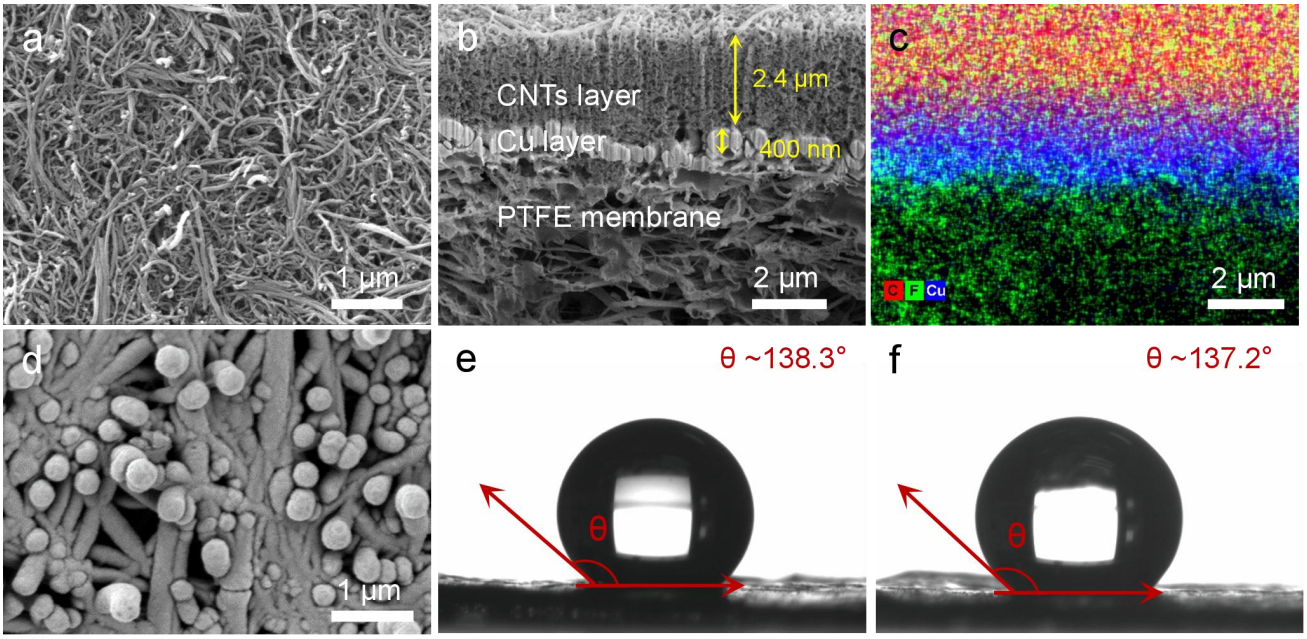

Fig. S12. (a) SEM image of CNTs, (b) SEM image (at 52° sample tilt), and (c) corresponding EDS elemental maps of the FIB-milled cross-section of the CNTs/CEI-Cu electrode. (d) SEM image of the underlying Cu of the CNTs/CEI-Cu electrode. Contact angles of the CNTs/CEI-Cu electrode (e) before and (f) after acidic CO_2 electrolysis at 300 mA cm^{-2} for 0.5 h.

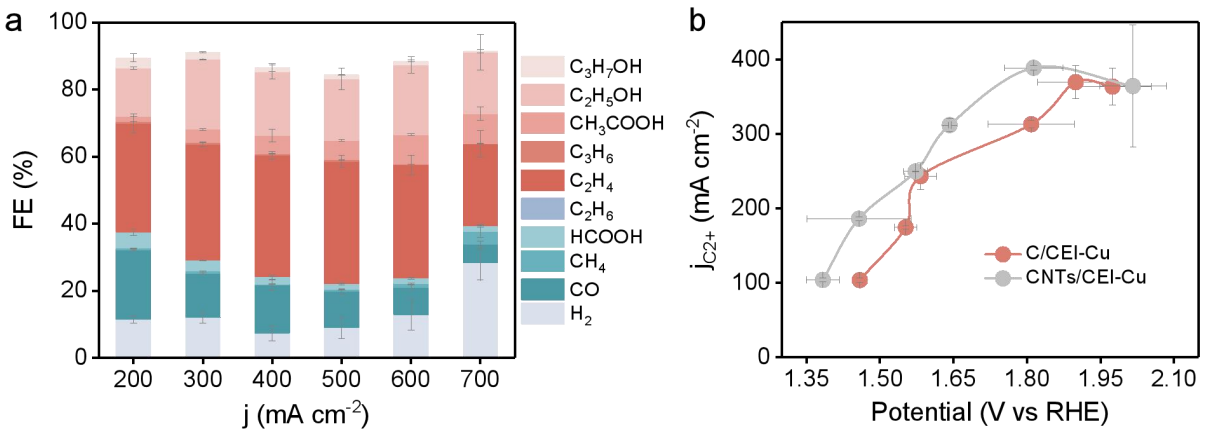

Fig. S13. (a) Product distributions for acidic CO_2 electrolysis on the CNTs/CEI-Cu electrode, and (b) j_{C2+} on C/CEI-Cu and CNTs/CEI-Cu electrodes as a function of working potential in 0.5 M K_2SO_4 (pH 2).

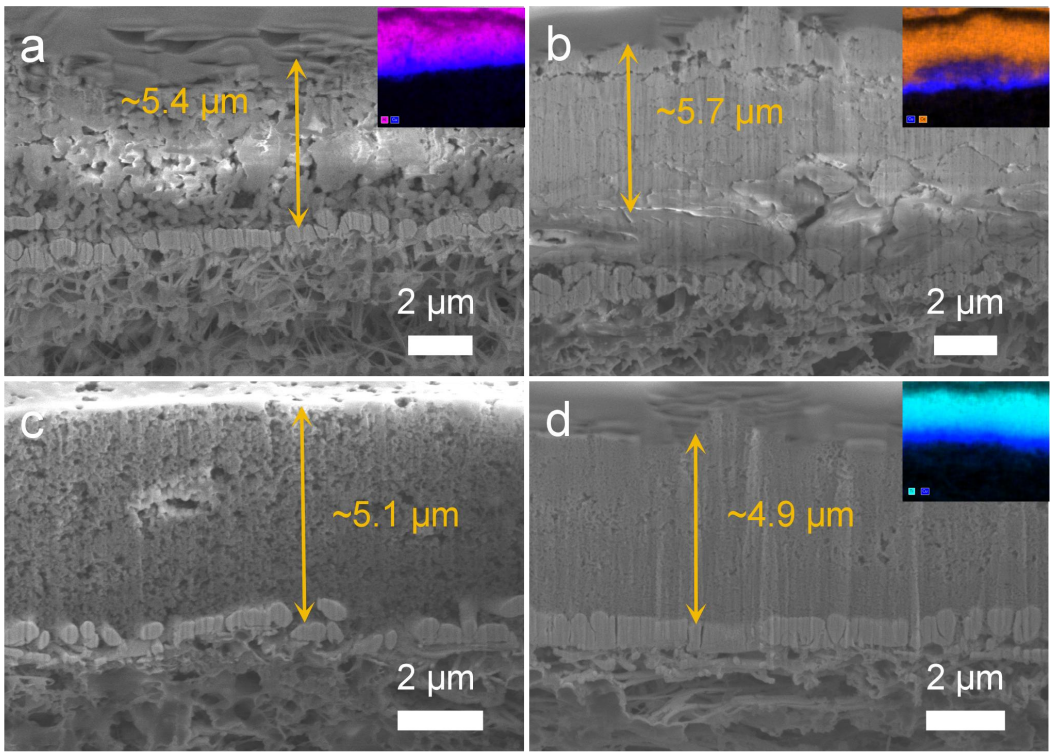

Fig. S14. SEM images (at 52° sample tilt) of the FIB-milled cross-section of (a) Al_2O_3/CEI-Cu, (b) CeO_2/CEI-Cu, (c) C/CEI-Cu, and (d) TiO_2/CEI-Cu electrodes. Insets show the corresponding overlaid metallic elemental maps.

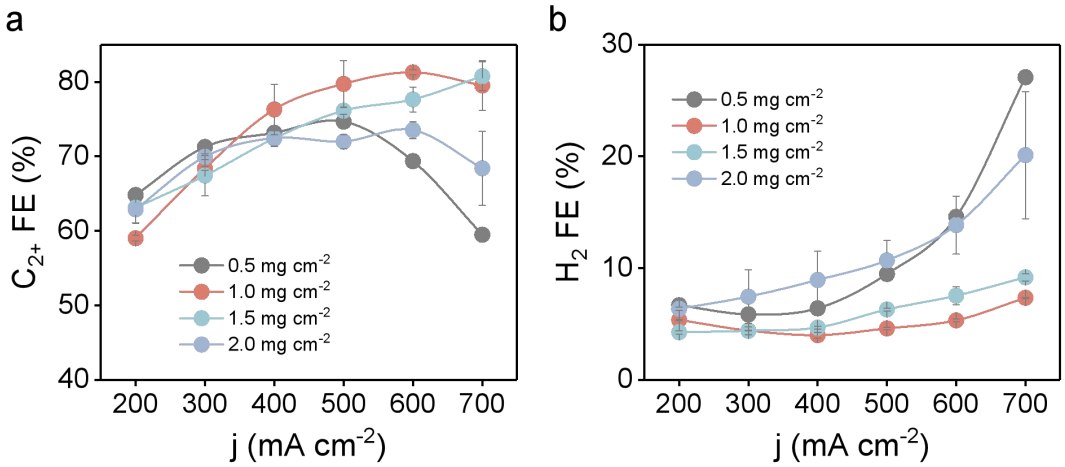

Fig. S15. FEs of (a) C_{2+} and (b) H_2 as a function of current density on Al_2O_3/CEI_{Low}-coated Cu electrodes with varying coating loadings in 0.5 M K_2SO_4 (pH 2). The electrode with a coating loading of 1.0 mg cm^{-2} referred to the electrode with a ~5 μm-thick Al_2O_3/CEI_{Low} coating. The thickness of the coating layer could influence the capacity for ion-flux regulation. A thinner coating layer failed to provide sufficient ion-flux regulation, resulting in poor CO_2-to-C_{2+} conversion. Increasing the coating layer thickness, however, did not lead to continuous performance improvement, as an excessively thick coating layer would introduce additional mass transport resistance for K^+ and CO_2.

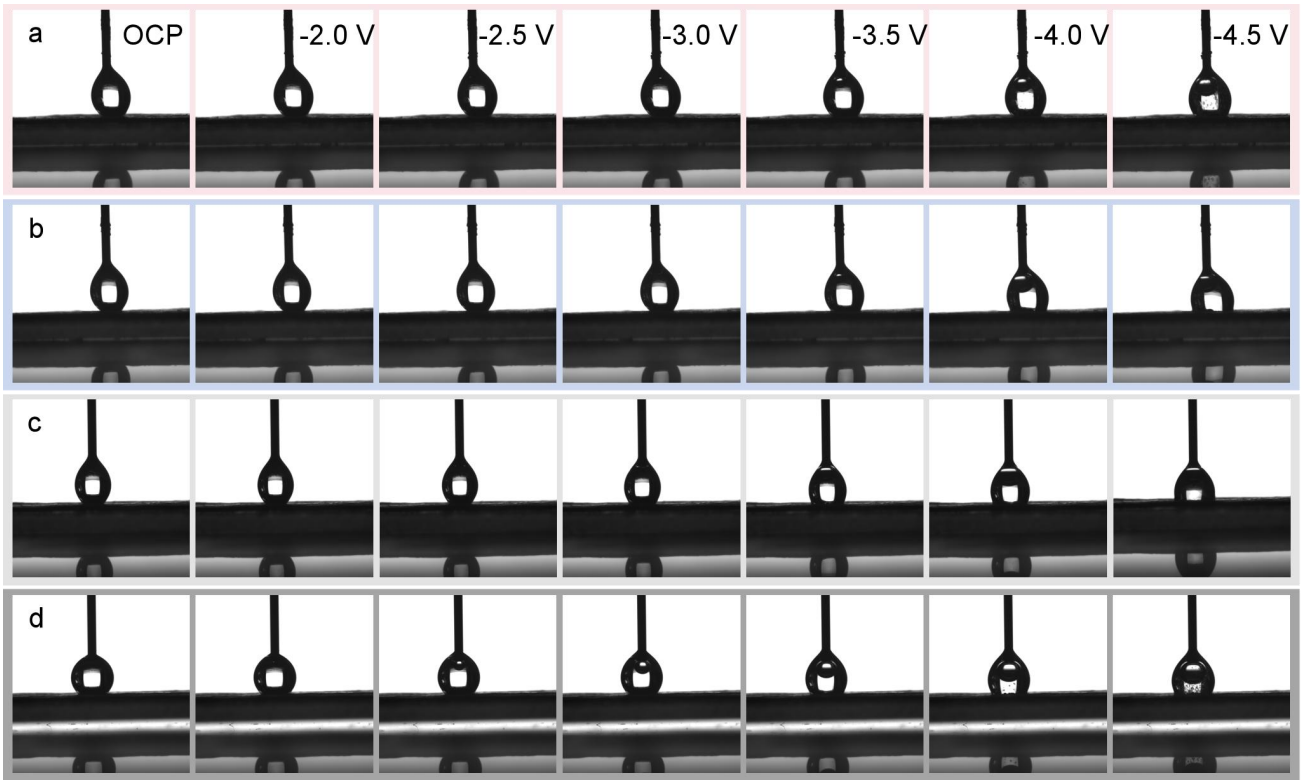

Fig. S16. *In situ* contact angle measurements of the electrolyte (0.5 M K_2SO_4, pH 2) on (a) Al_2O_3/CEI-Cu, (b) CeO_2/CEI-Cu, (c) C/CEI-Cu, and (d) TiO_2/CEI-Cu electrodes under OCP and applied voltages (between the electrode and syringe needle).

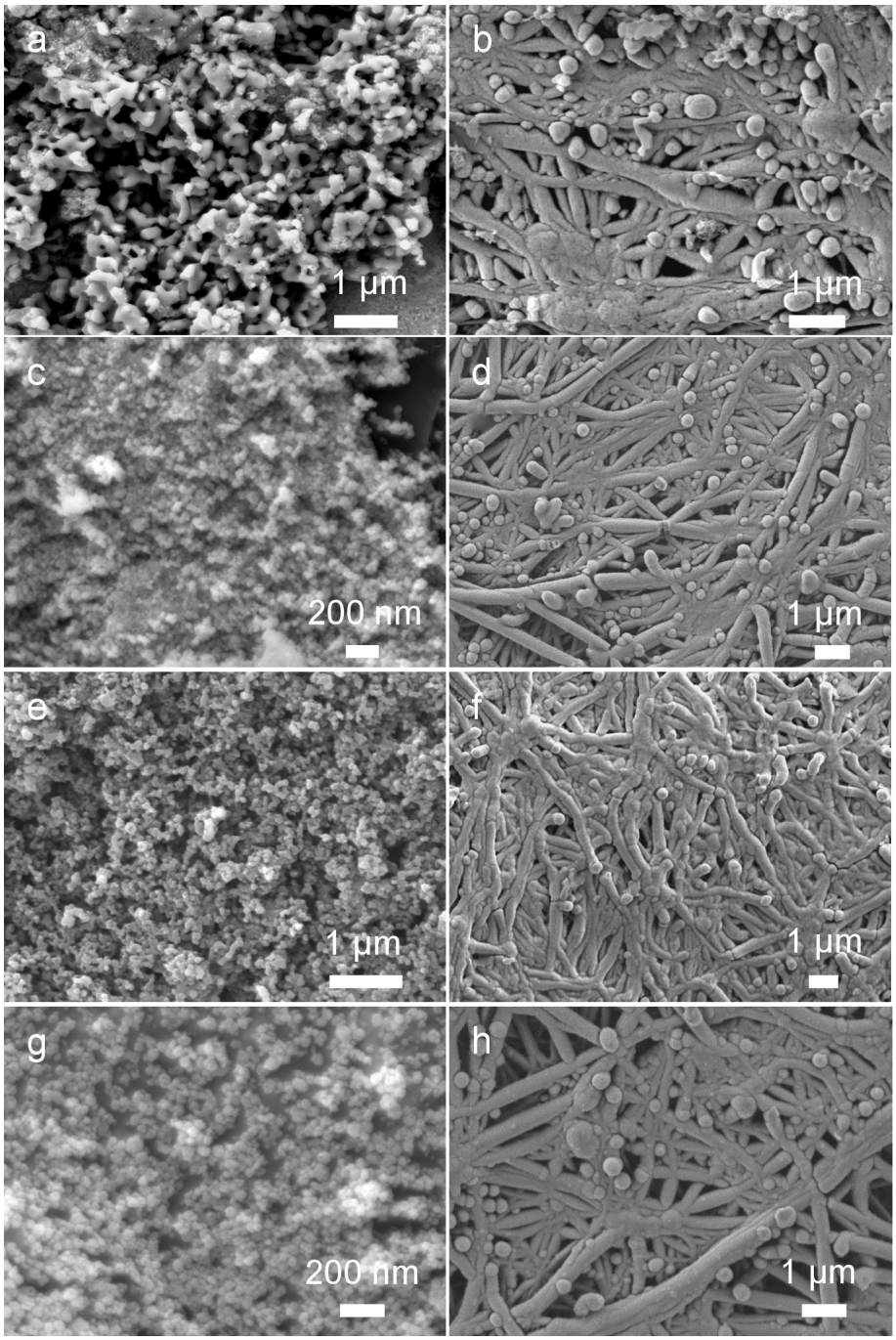

Fig. S17. SEM images of the fillers: (a) Al_2O_3, (c) CeO_2, (e) carbon, and (g) TiO_2. SEM images of the underlying Cu of the corresponding electrodes: (b) Al_2O_3/CEI-Cu, (d) CeO_2/CEI-Cu, (f) C/CEI-Cu, and (h) TiO_2/CEI-Cu.

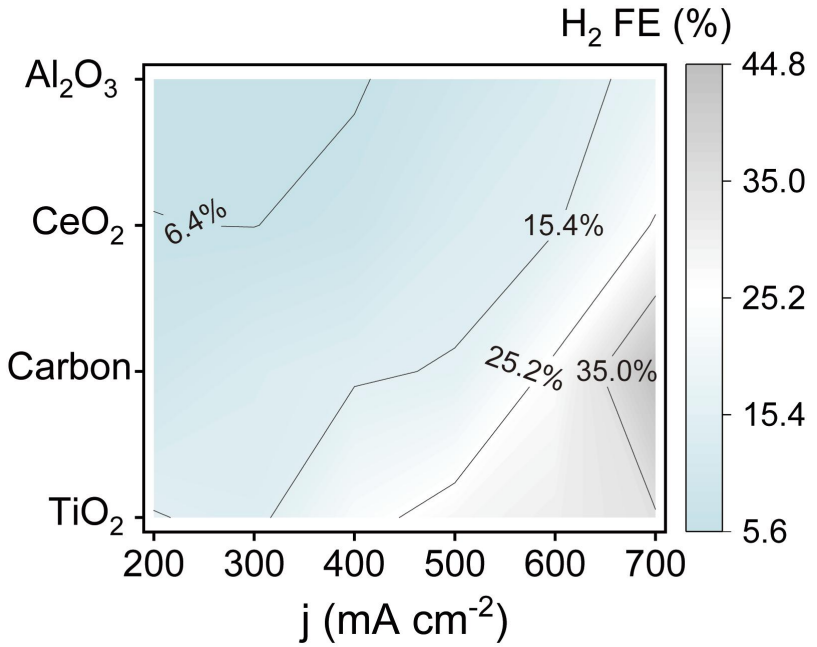

Fig. S18. Contour plot of H_2 FE as a function of current density and inorganic filler type in 0.5 M K_2SO_4 (pH 2).

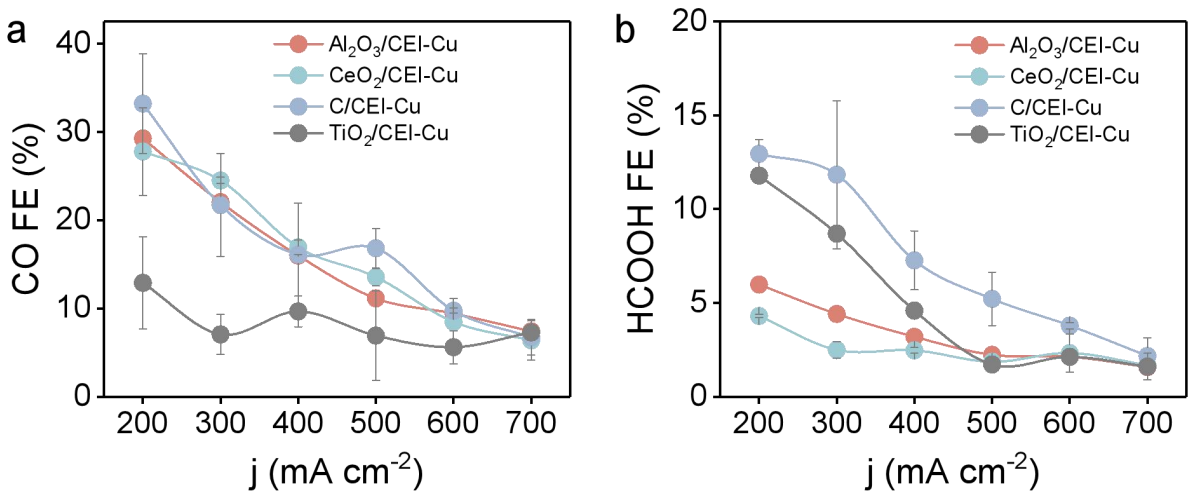

Fig. S19. FEs of (a) CO and (b) HCOOH as a function of current density on various electrodes in 0.5 M K_2SO_4 (pH 2).

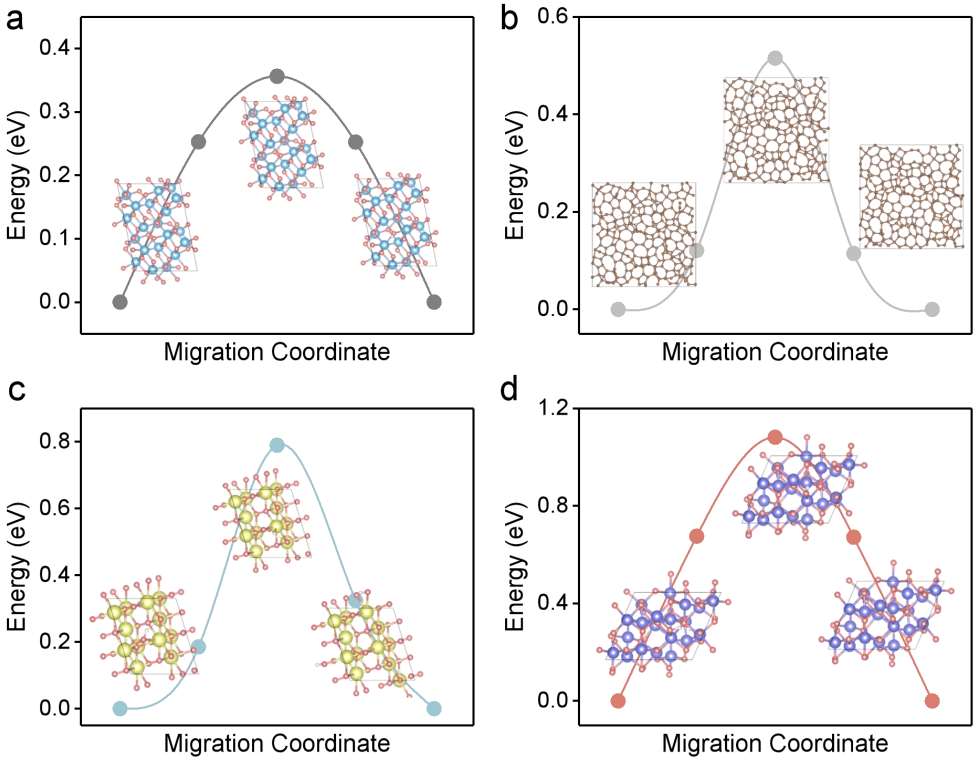

Fig. S20. Computed H-migration profiles on (a) TiO_2, (b) Carbon, (c) CeO_2, and (d) Al_2O_3 surfaces.

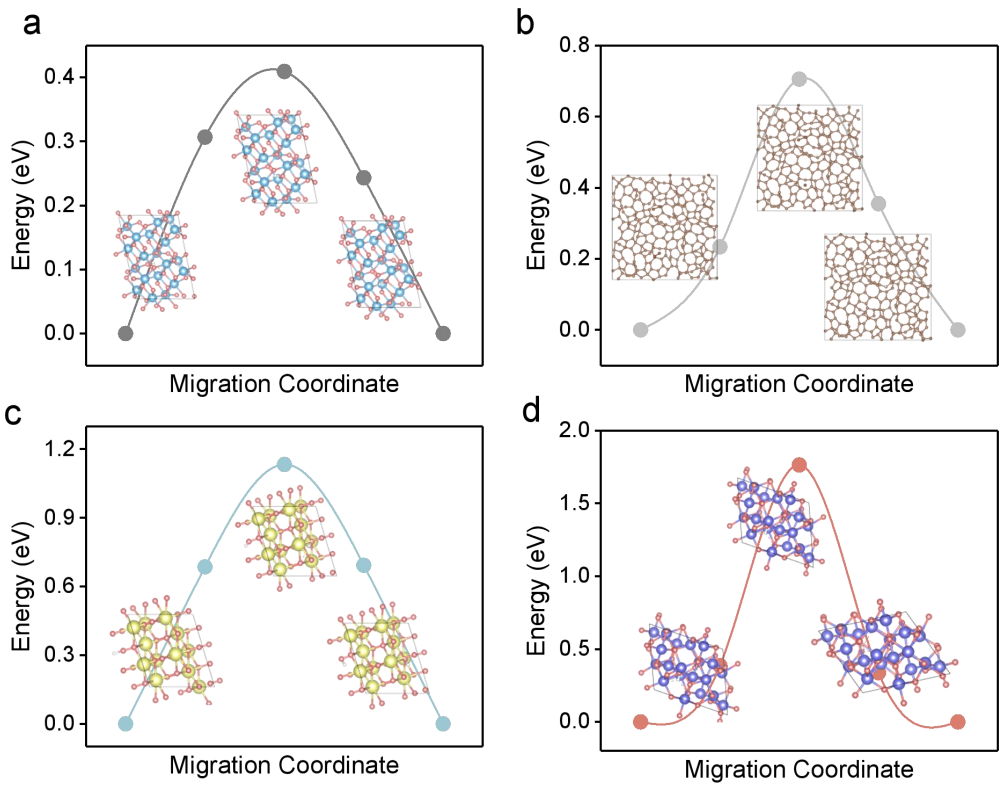

Fig. S21. Computed H-migration profiles within the bulk of (a) TiO_2, (b) Carbon, (c) CeO_2, and (d) Al_2O_3.

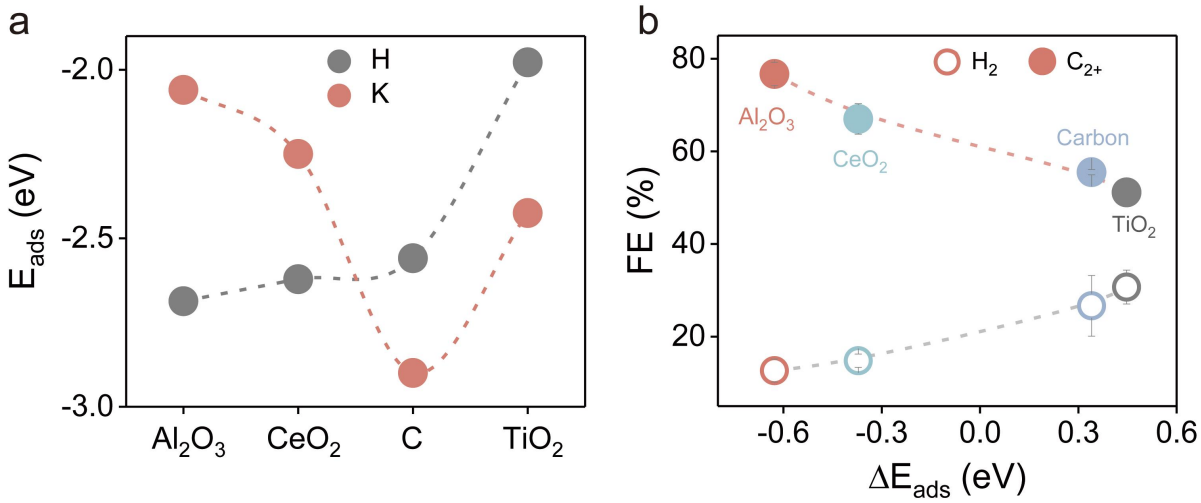

Fig. S22. (a) Computed adsorption energies of H and K on the surface of various inorganic fillers. (b) H_2 and C_{2+} FEs at 600 mA cm^{-2} as a function of ΔE_{ads} ($E_{ads, H} - E_{ads, K}$) for various inorganic fillers.

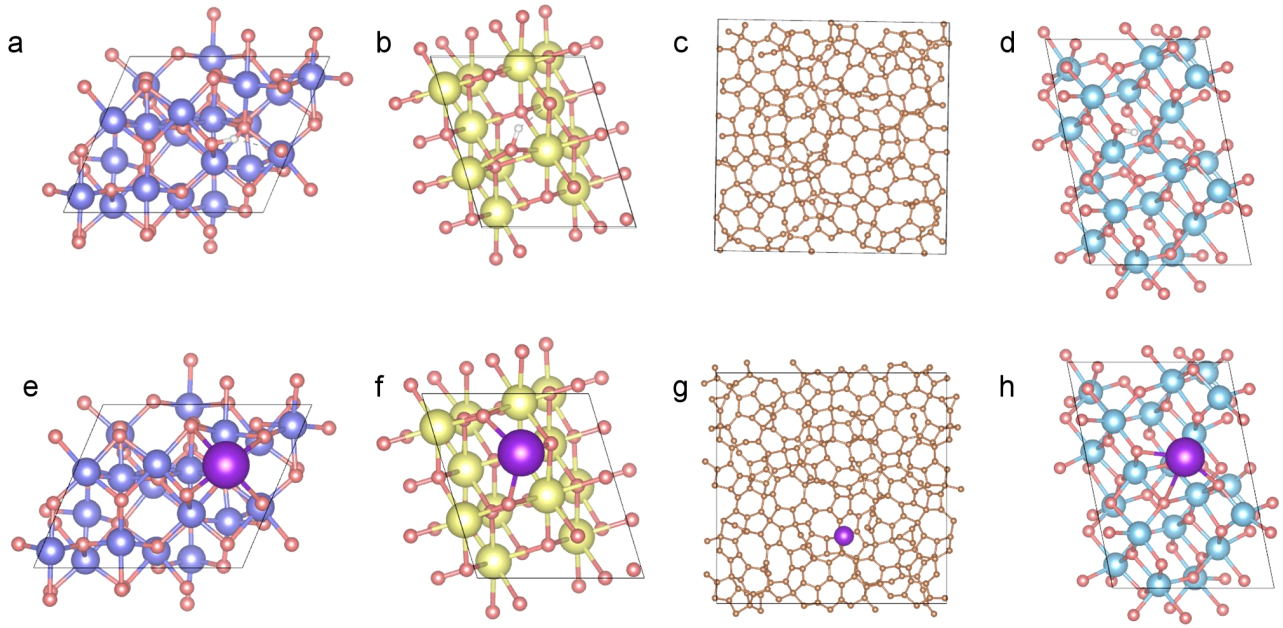

Fig. S23. Optimized configurations with (a-d) adsorbed H and (e-h) adsorbed K on (a, e) Al_2O_3, (b, f) CeO_2, (c, g) carbon, (d, h) TiO_2 surface.

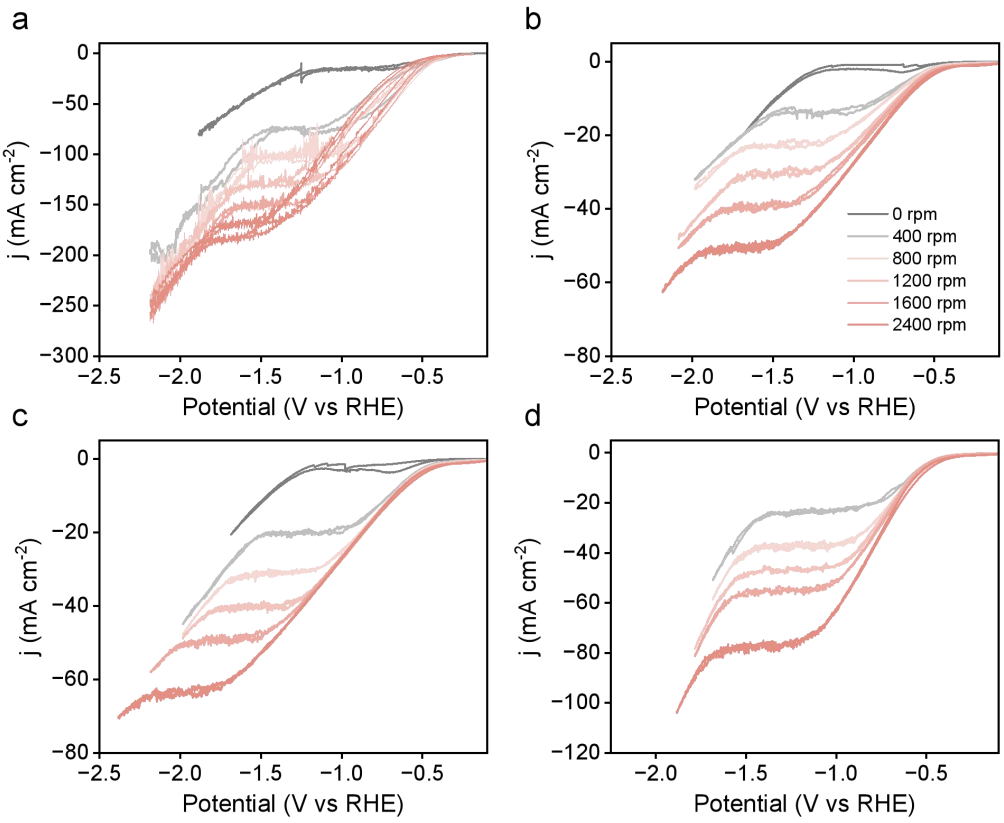

Fig. S24. CV curves of (a) Cu RDE, (b) Al_2O_3/CEI-Cu RDE, (c) CeO_2/CEI-Cu RDE, and (d) TiO_2/CEI-Cu RDE in Ar-saturated 0.5 M K_2SO_4 (pH 2) at various rotation rates. Scan rate: 50 mV s^{-1}.

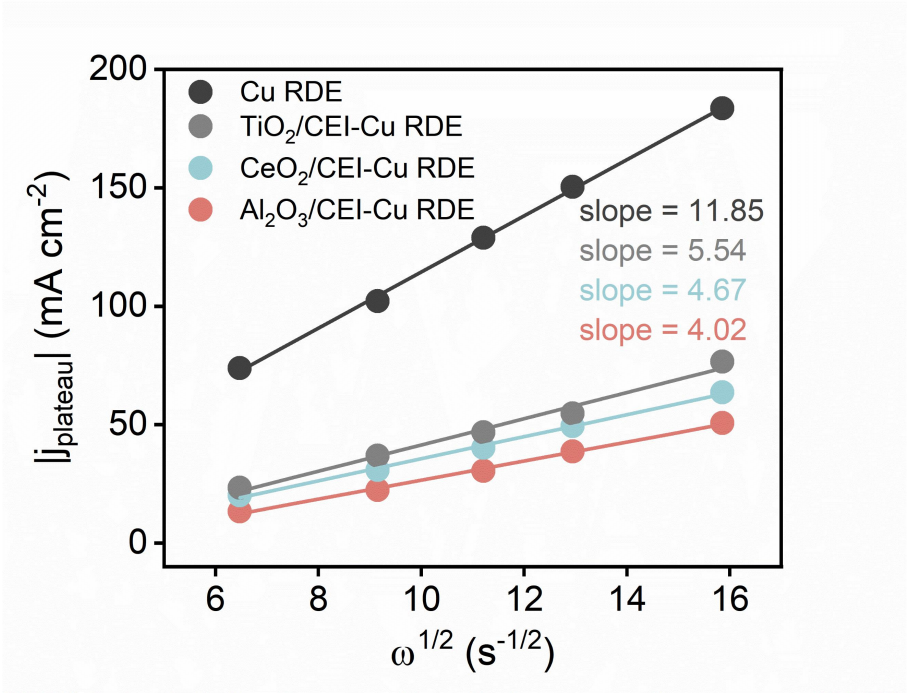

Fig. S25. Linear fitting of $|j_{plateau}|$ vs $\omega^{1/2}$ for Cu and coated Cu RDE.

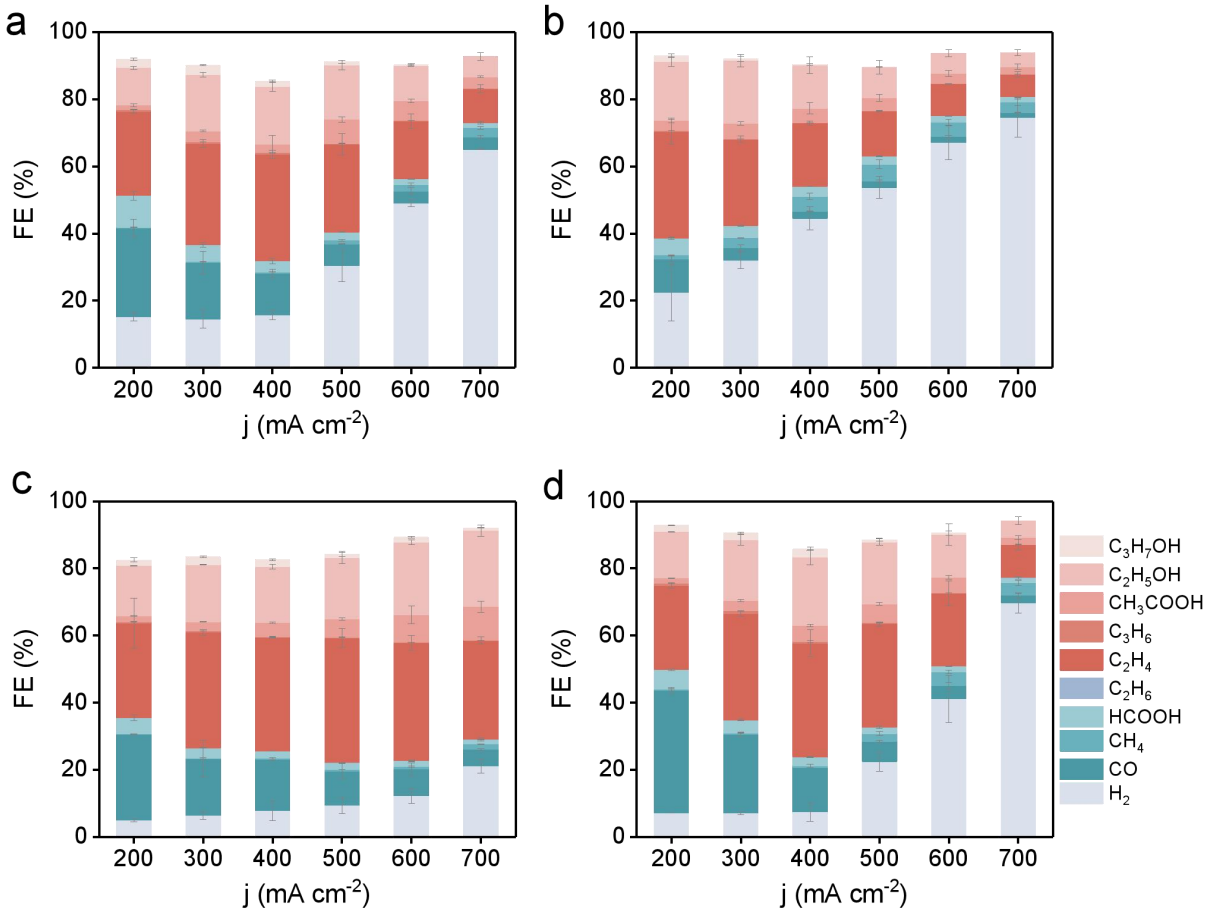

Fig. S26. Product distributions for acidic CO_2 electrolysis on (a) C/NI-Cu, (b) C/AEI-Cu, (c) Al_2O_3/NI-Cu, and (d) Al_2O_3/AEI-Cu electrodes in 0.5 M K_2SO_4 (pH 2).

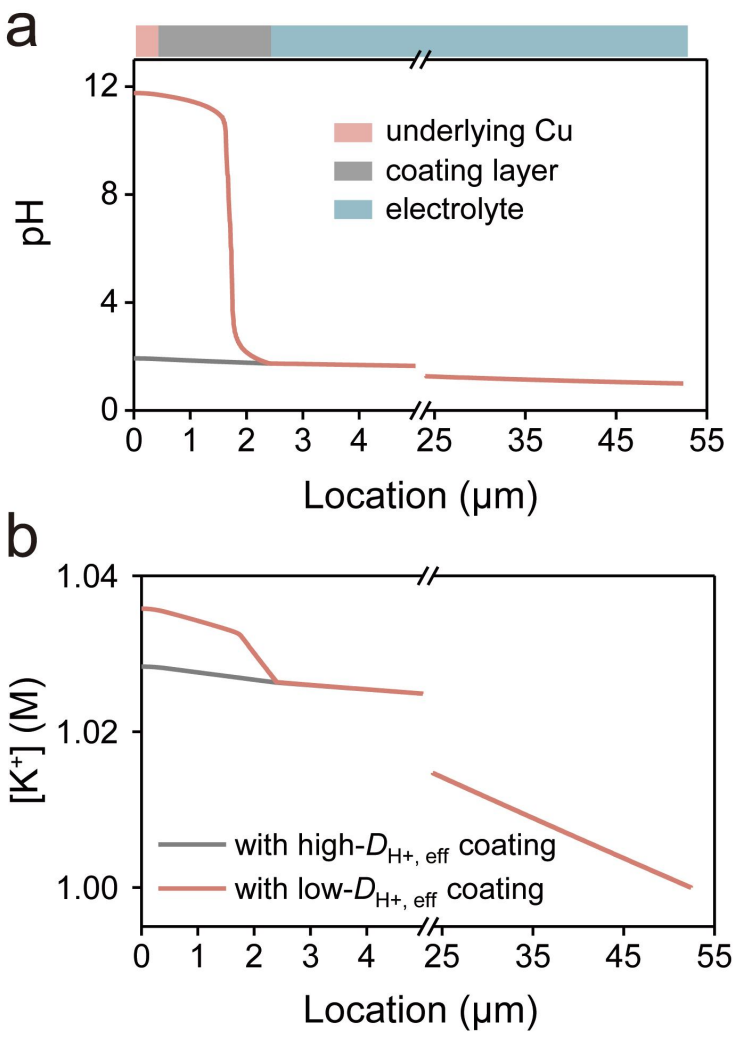

Fig. S27. Simulated (a) pH profiles and (b) K^+ concentration ($[K^+]$) profiles from the electrode surface to the bulk electrolyte for coated Cu electrodes with varying proton diffusion coefficients ($D_{H+, eff}$) of the coating at a current density of 150 mA cm^{-2}.

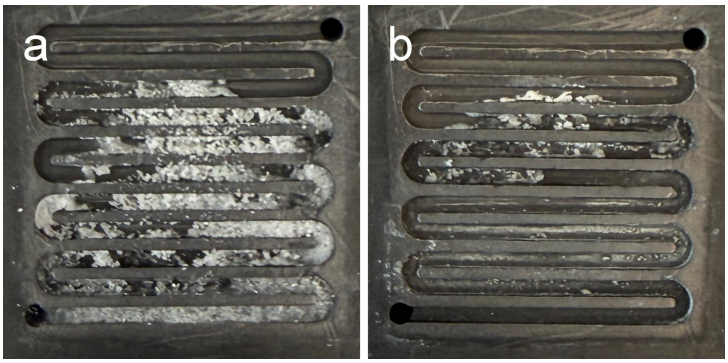

Fig. S28. Optical photographs of the gas channel after the durability test in (a) 0.5 M K_2SO_4 for 70 h and (b) 0.1 M K_2SO_4 for 200 h.

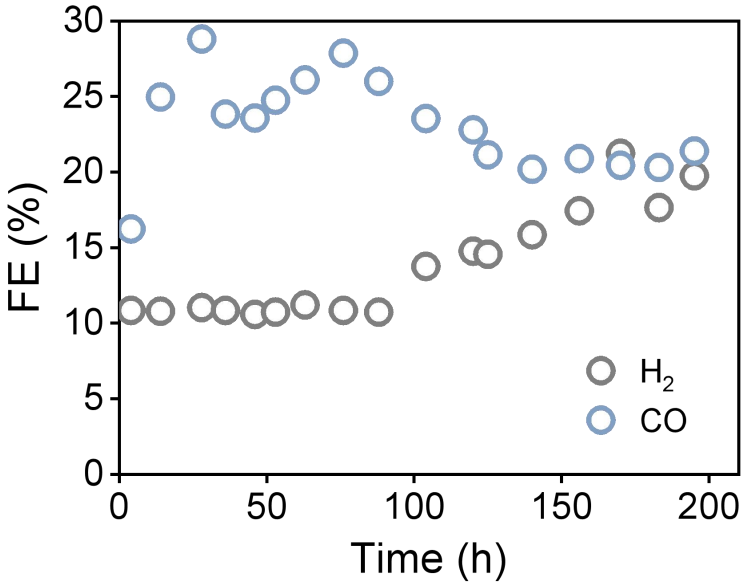

Fig. S29. Time-dependent FEs of CO and H_2 during long-term testing in 0.1 M K_2SO_4 (pH 2).

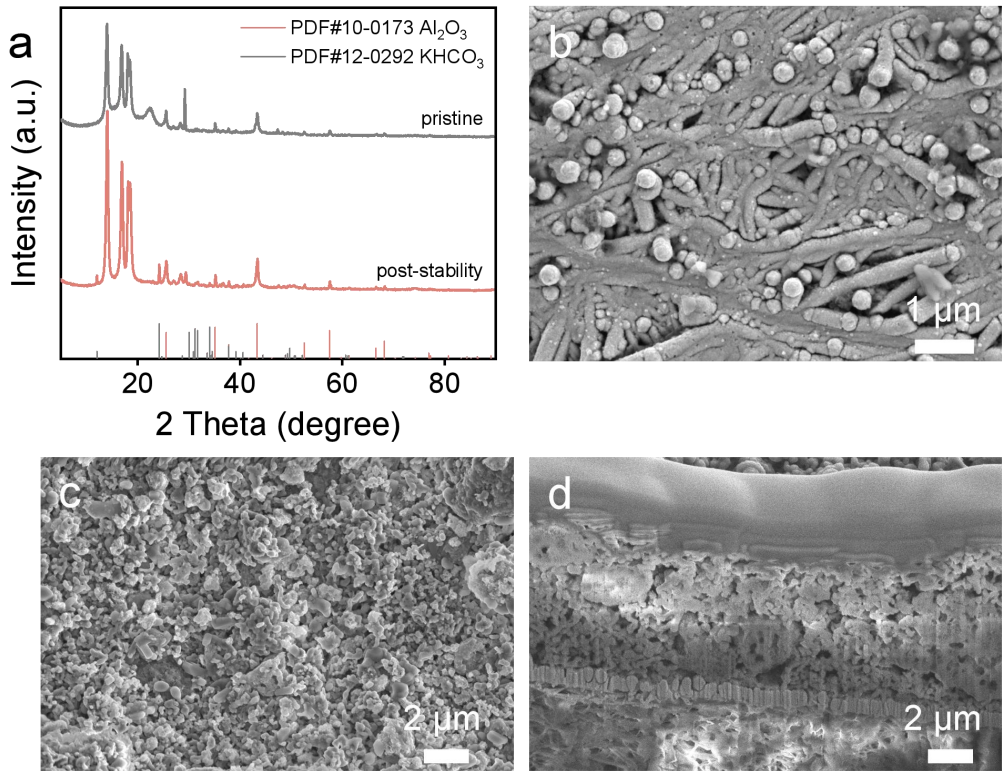

Fig. S30. (a) XRD patterns of the Al_2O_3/CEI_{Low}-Cu electrode before and after a 200-h durability test at 200 mA cm^{-2} in 0.1 M K_2SO_4 (pH 2). (b, c) SEM images of (b) the underlying Cu of the electrode and (c) the electrode surface after the durability test. (d) SEM image (at 52° sample tilt) of the FIB-milled cross-section of the electrode after the durability test.

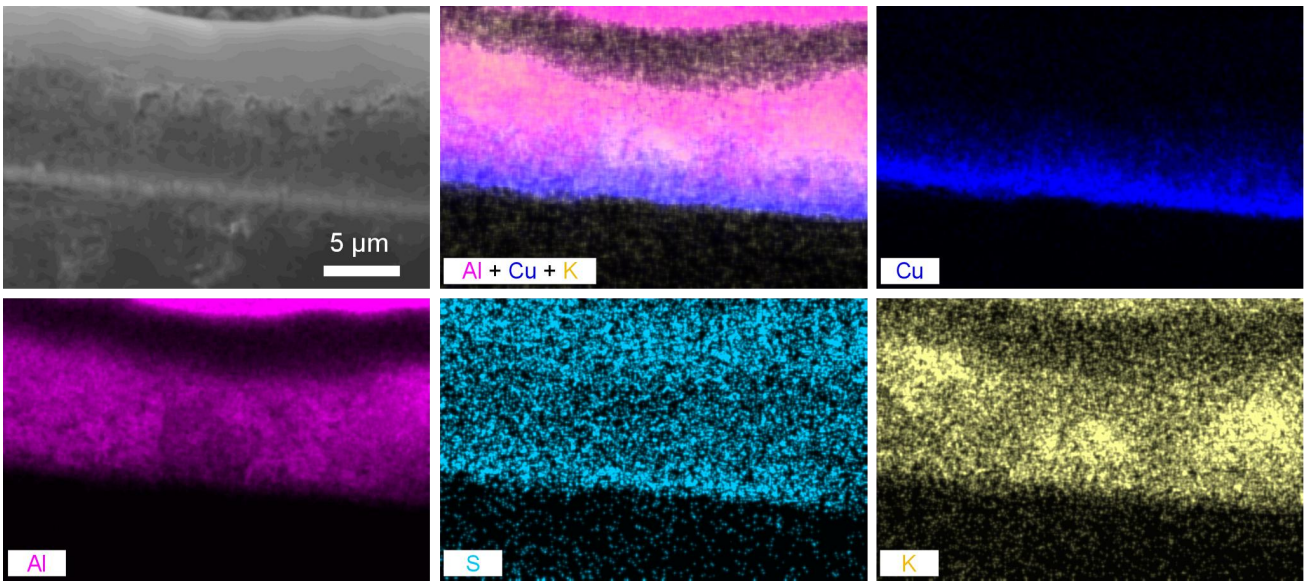

Fig. S31. SEM image (at 52° sample tilt) and corresponding EDS elemental maps of the FIB-milled cross-section of the Al_2O_3/CEI_{Low}-Cu electrode after a 200-h durability test.

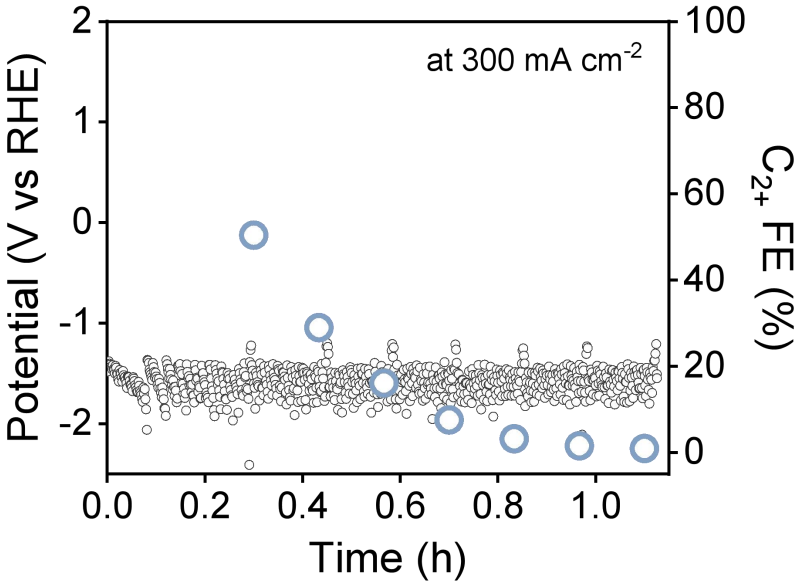

Fig. S32. Durability test of the Cu electrode at 300 mA cm^{-2} in 0.5 M K_2SO_4 (pH 2).

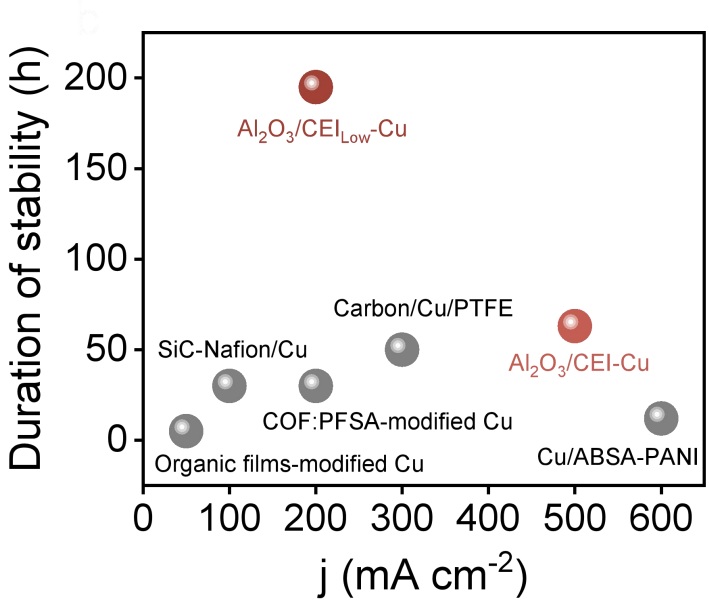

Fig. S33. Comparison of the duration of stability with previously reported electrode coating formulation.

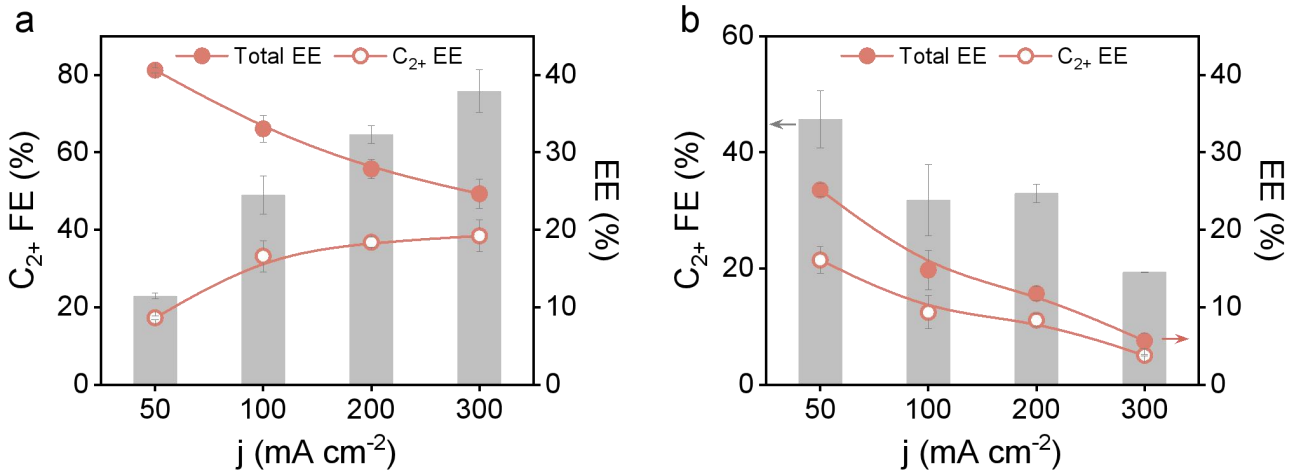

Fig. S34. EEs for total CO_2 electrolysis products and C_{2+} products, together with C_{2+} FE, as a function of current density on (a) Al_2O_3/CEI-Cu and (b) Cu electrodes in 0.5 M K_2SO_4 (pH 2).

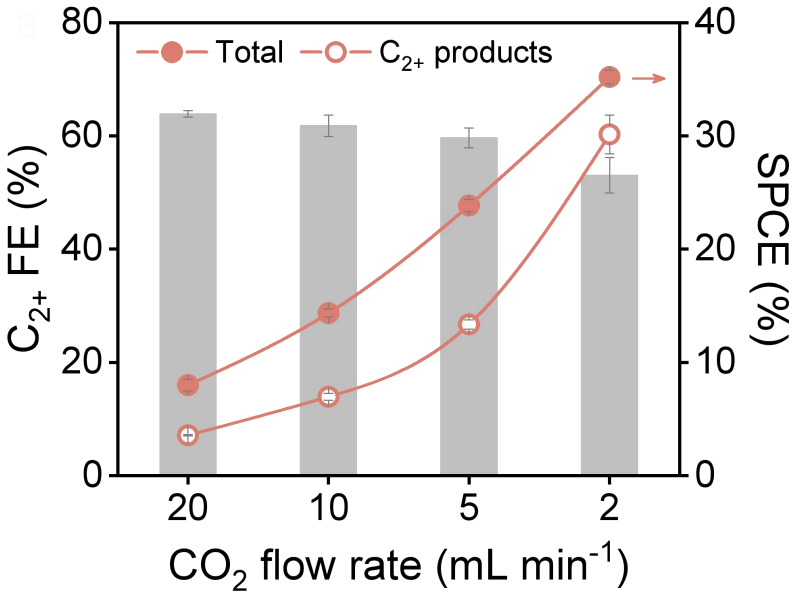

Fig. S35. FE and SPCE for C_{2+} products, as well as SPCE for total CO_2 electrolysis products, as a function of CO_2 flow rate at 200 mA cm^{-2}.

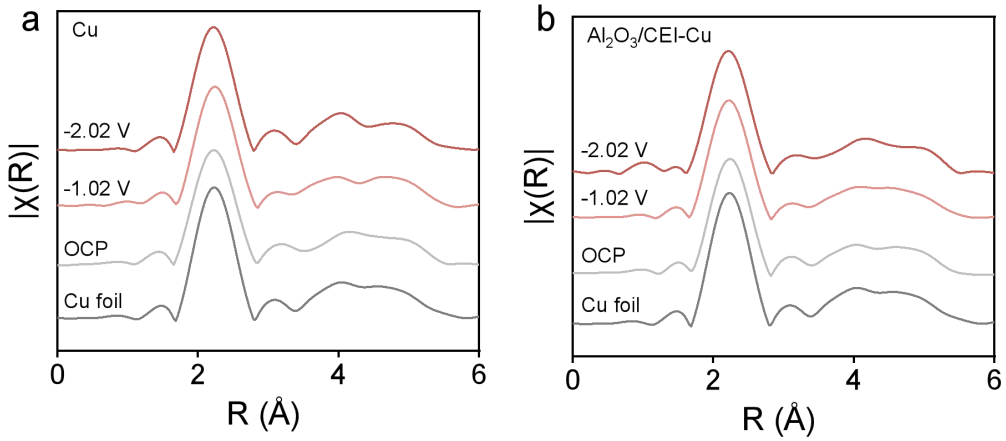

Fig. S36. *In situ* Cu K-edge Fourier-transformed extended X-ray absorption fine structure (EXAFS) spectra of (a) Cu and (b) Al_2O_3/CEI-Cu electrodes at OCP, –1.02 and –2.02 V vs Ag/AgCl in CO_2-saturated 0.5 M K_2SO_4 (pH 2), with Cu foil as a reference.

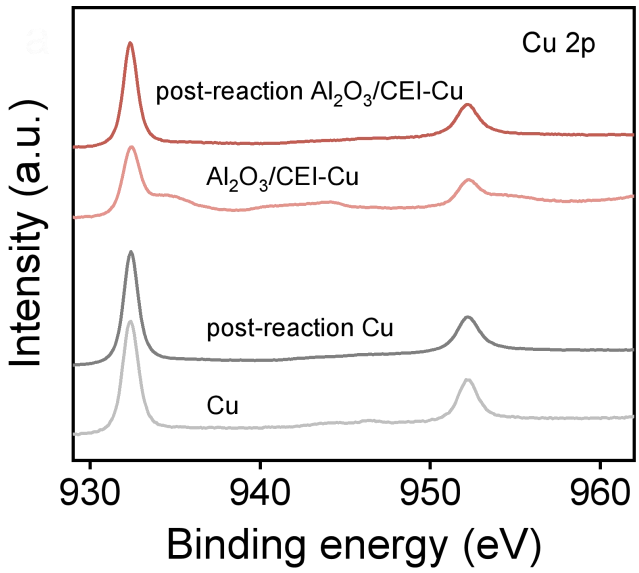

Fig. S37. Cu 2p XPS spectra of Cu and Al_2O_3/CEI-Cu electrodes, measured quasi-*in situ* before and after 30 min of CO_2 electrolysis at 400 mA cm^{-2} in 0.5 M K_2SO_4 (pH 2).

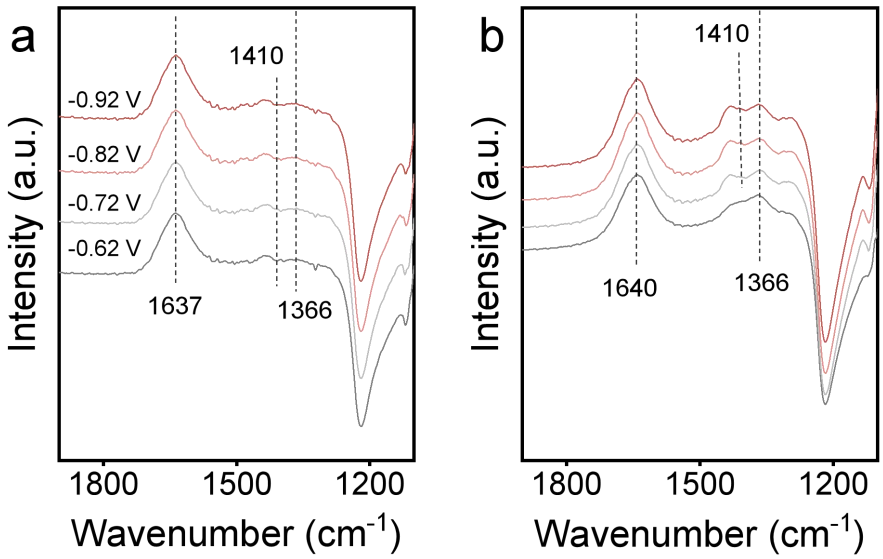

Fig. S38. *In situ* ATR-SEIRAS spectra of (a) Cu and (b) Al_2O_3/CEI-Cu electrodes in the range of 1900–1100 cm^{-1} at applied potentials.

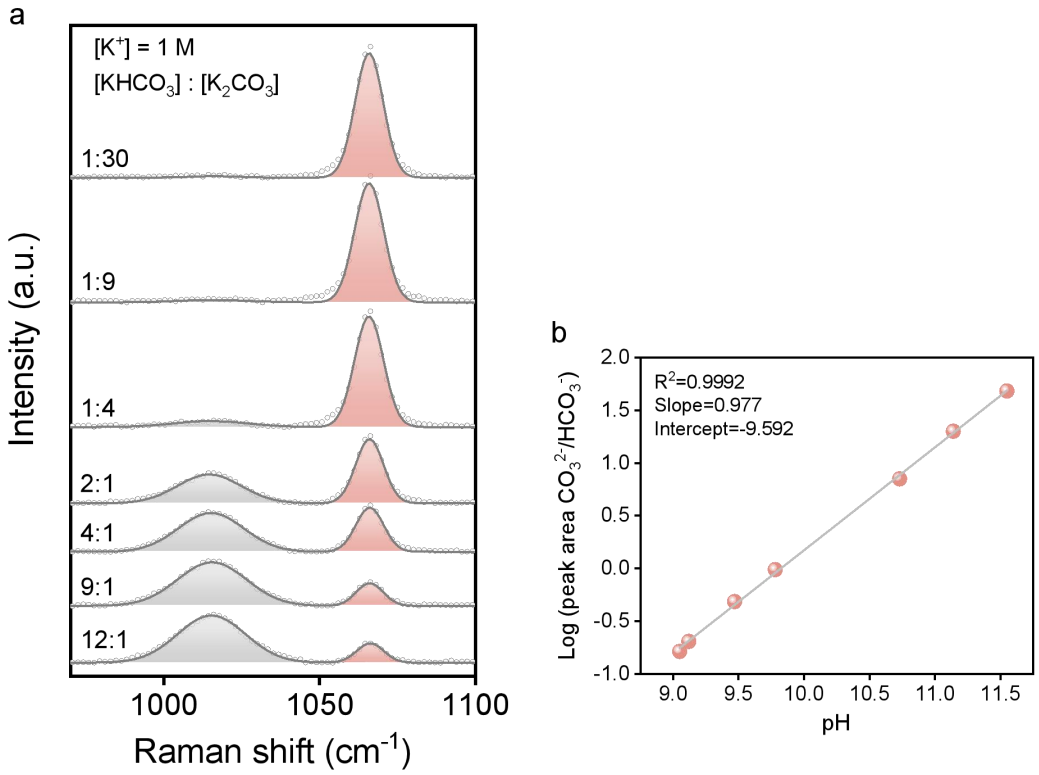

Fig. 39. (a) Raman spectra of calibration solutions with different pHs. All solutions contained 1 M K^+ with varying CO_3^{2-}/HCO_3^- molar ratio. (b) Calibration curve for local pH utilizing the logarithm of the Raman peak area ratio of CO_3^{2-} to HCO_3^-.

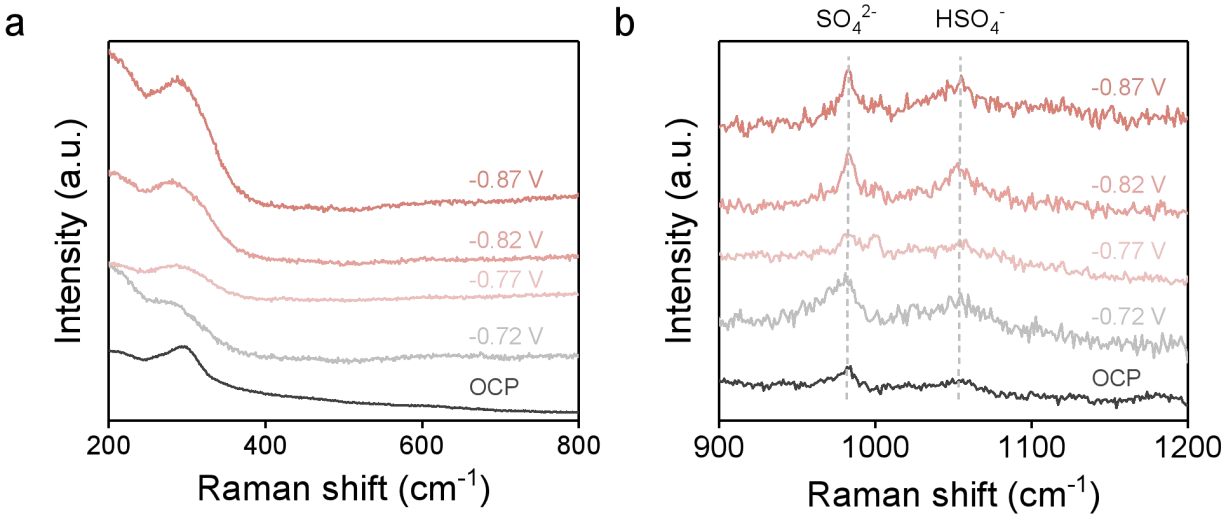

Fig. S40. *In situ* Raman spectra of the Al_2O_3/CEI-Cu electrode in the ranges of (a) 200–800 cm^{-1} and (b) 900–1200 cm^{-1} at OCP and applied potentials under an Ar atmosphere.

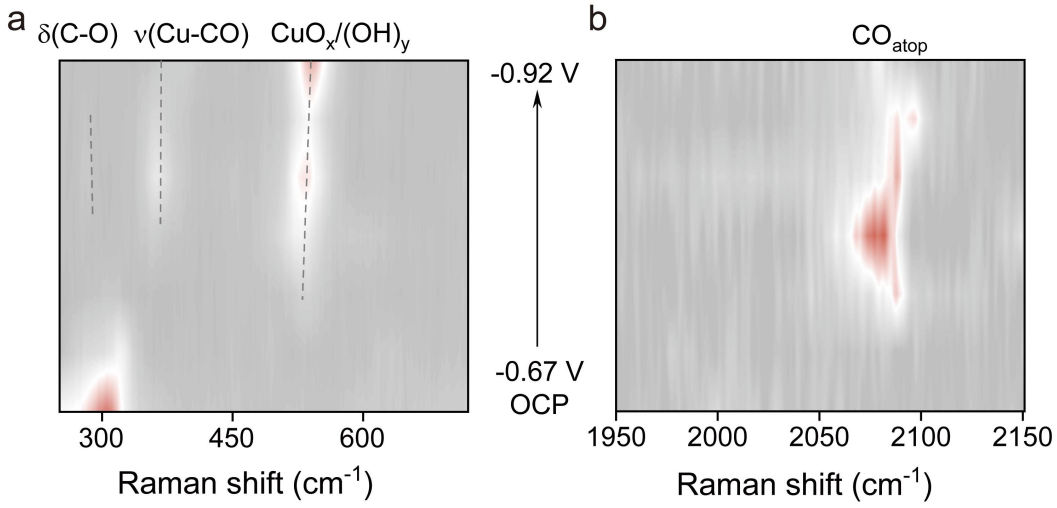

Fig. S41. *In situ* Raman spectra of the Al_2O_3/CEI-Cu electrode in the ranges of (a) 200–800 cm^{-1} and (b) 1950–2150 cm^{-1} at OCP and applied potentials.

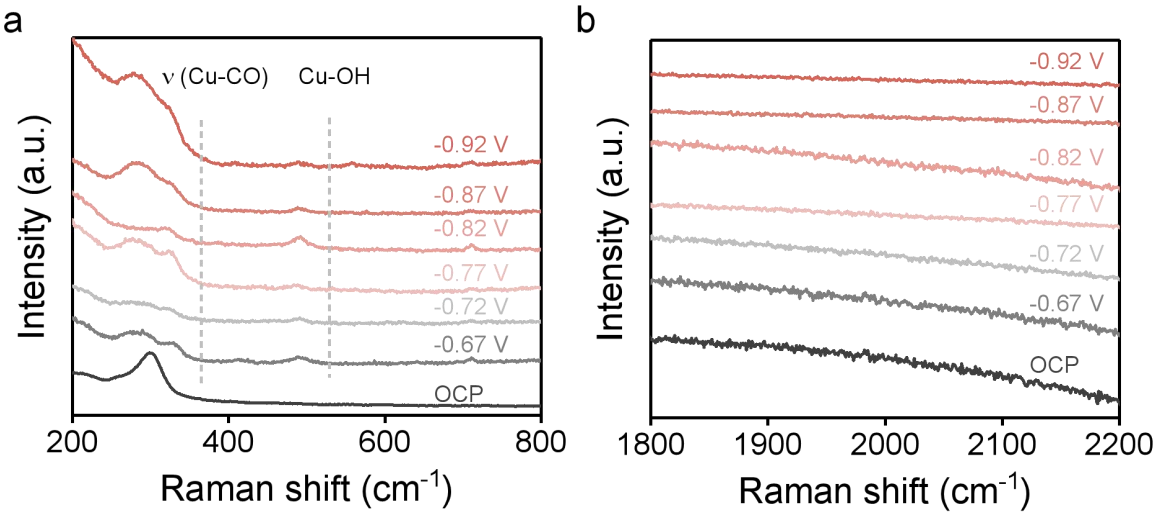

Fig. S42. *In situ* Raman spectra of the Cu electrode in the ranges of (a) 200–800 cm^{-1} and (b) 1800–2200 cm^{-1} at OCP and applied potentials.

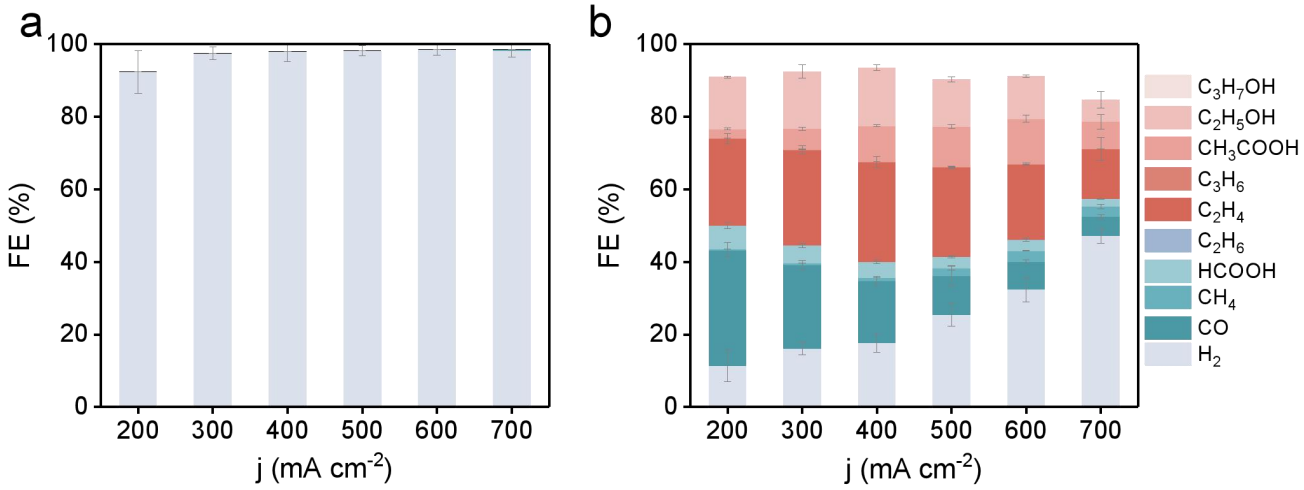

Fig. S43. Product distributions for acidic CO_2 electrolysis on (a) Cu and (b) Al_2O_3/CEI-Cu electrodes in 0.5 M K_2SO_4 (pH 1).

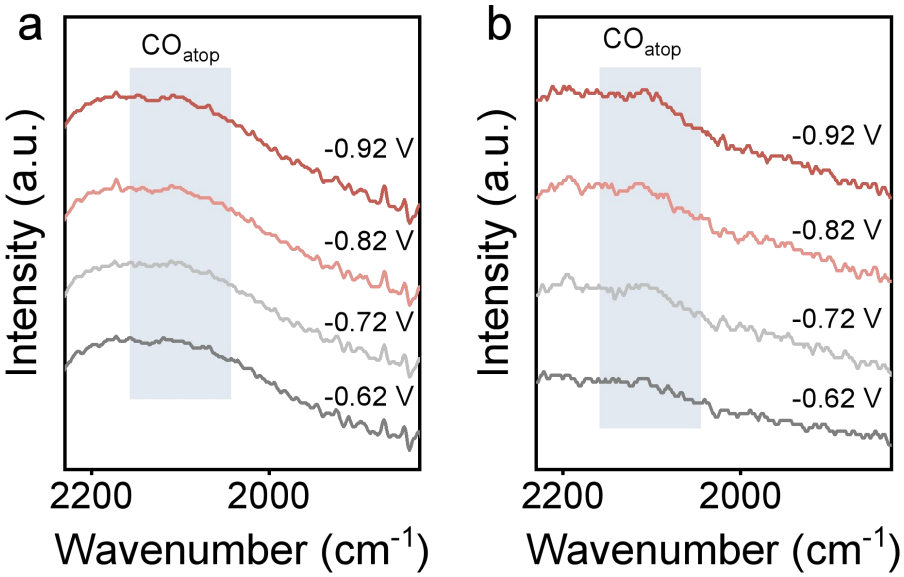

Fig. S44. *In situ* ATR-SEIRAS spectra of (a) Cu and (b) Al_2O_3/CEI-Cu electrodes in the range of 2230–1830 cm^{-1} at applied potentials.

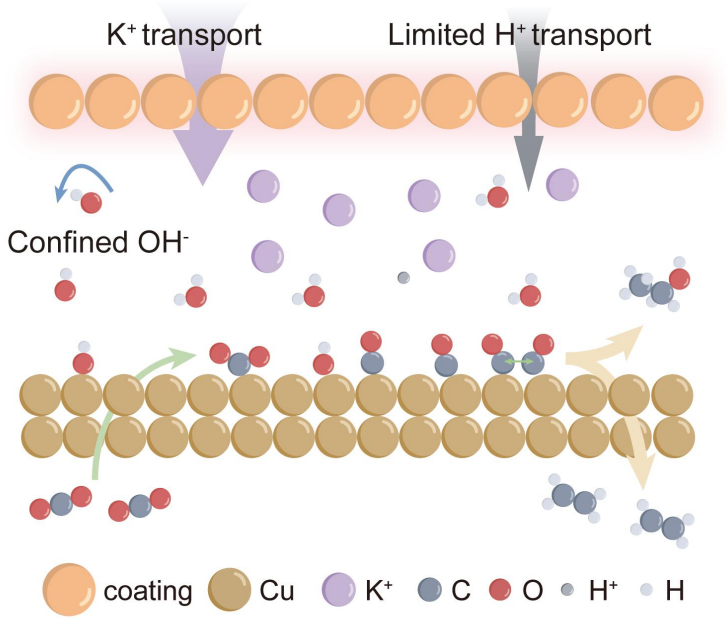

Fig. S45. Schematic illustration of ion-flux regulation and the resulting interfacial microenvironment on the coated Cu electrode.

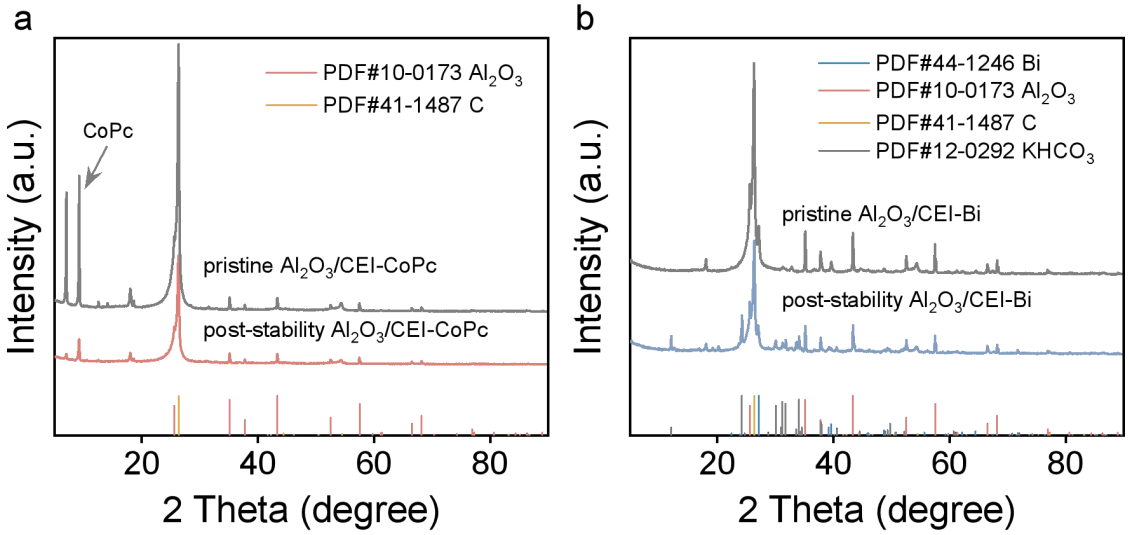

Fig. S46. XRD patterns of (a) Al_2O_3/CEI-CoPc and (b) Al_2O_3/CEI-Bi electrodes before and after the durability test.

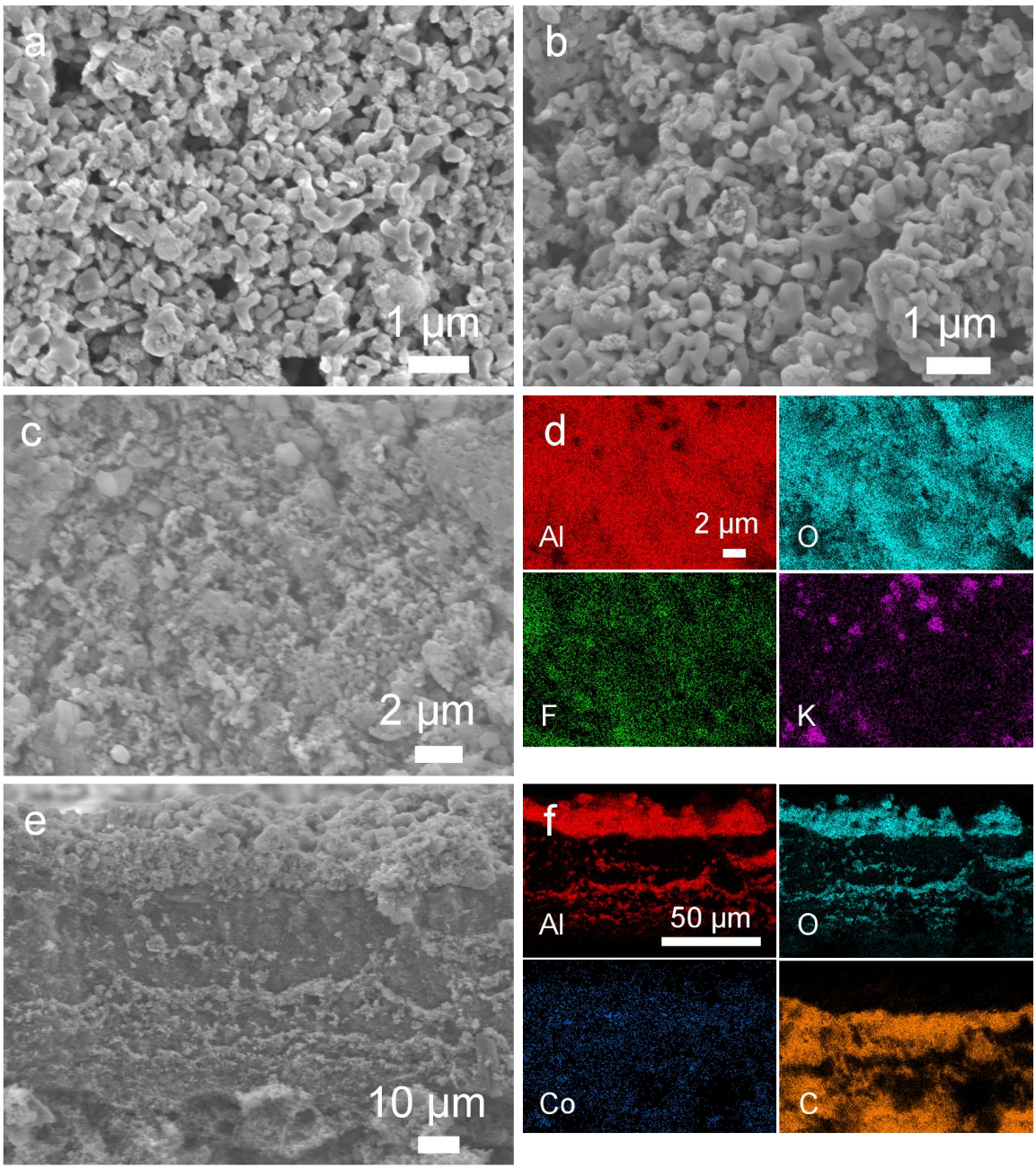

Fig. S47. SEM images of the Al_2O_3/CEI-CoPc electrode (a) before and (b) after the durability test. SEM images and corresponding EDS elemental maps of the Al_2O_3/CEI-CoPc electrode after the durability test: (c, d) surface view and (e, f) cross-sectional view.

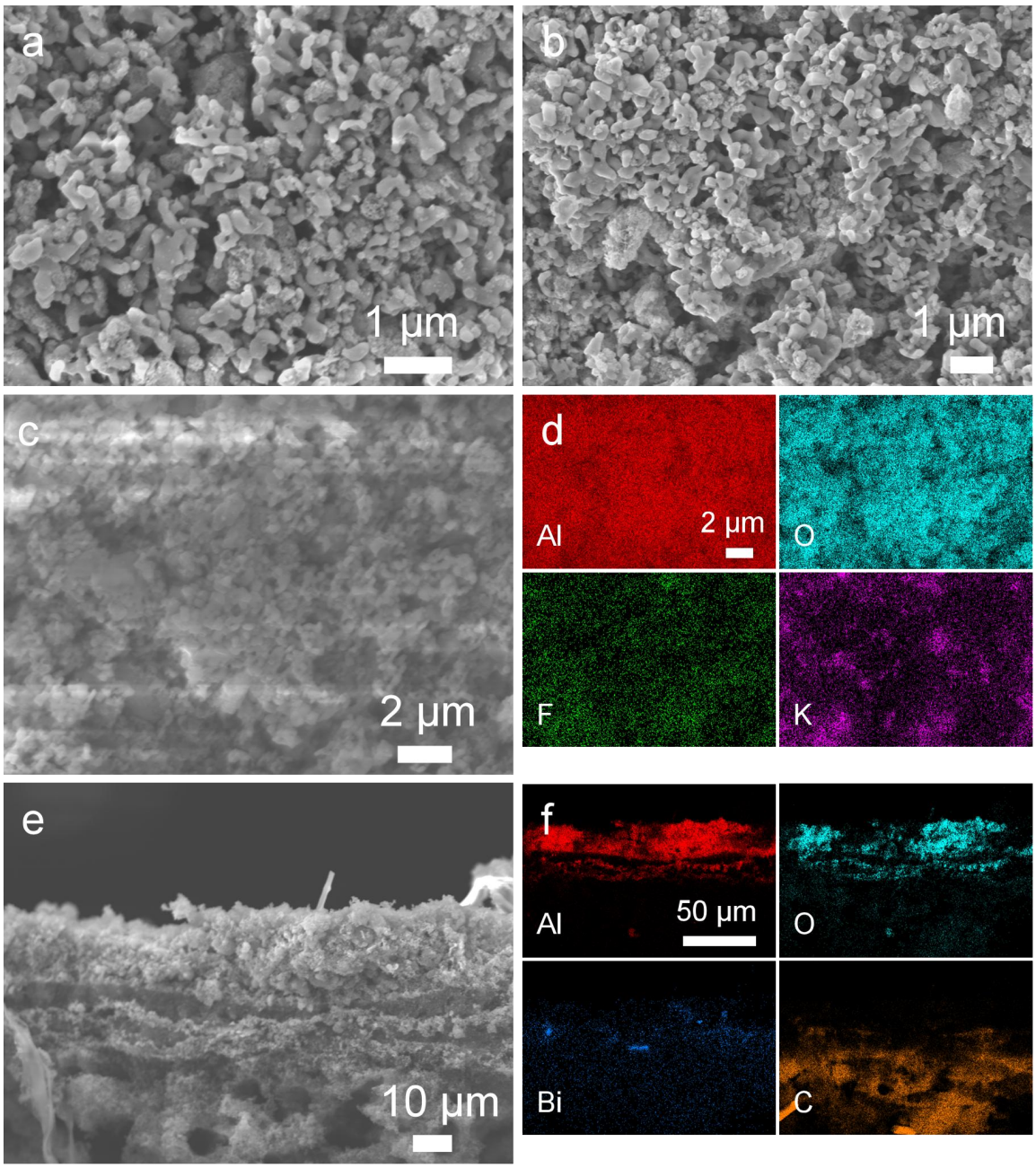

Fig. S48. SEM images of the Al_2O_3/CEI-Bi electrode (a) before and (b) after the durability test. SEM images and corresponding EDS elemental maps of the Al_2O_3/CEI-Bi electrode after the durability test: (c, d) surface view and (e, f) cross-sectional view.

Table S4. Porosity of various coating layers and C_{2+} FE at 600 mA cm^{-2} on the corresponding coated Cu electrodes. Notably, within the nanoscale regime (40–200 nm), the variation in coating porosity cannot be solely attributed to particle size, as factors, e.g., particle aggregation, size distribution, and coating formation process, also play important roles. Consequently, coatings with similar filler sizes exhibited markedly different porosities. Moreover, no clear correlation between porosity and catalytic performance was observed.

Coating	C/CEI	CNTs/CEI	Al_2O_3/CEI	CeO_2/CEI	TiO_2/CEI
Porosity	70.6%	78.9%	80.2%	32.0%	65.3%
C_{2+} FE at 600 mA cm^{-2}	61.5% (~2.3 μm) 55.5% (~5 μm)	64.8% (~2 μm)	76.7% (~5 μm)	67% (~5 μm)	51.2% (~5 μm)

Table S5. Comparison of the acidic CO_2 electrolysis performance for Al_2O_3/CEI_{Low}-Cu electrode with previously reported catalysts under acidic conditions.

Reference	Catalyst	Electrolyte	$FE_{C2+, max}$ (%)	$j_{C2+, max}$ (mA cm^{-2})	Stability (h)	SPCE (%)
Our work	Al_2O_3/CEI_{Low}-Cu	0.5 M K_2SO_4 (pH 2)	81.3	556.6	63 at 500 mA cm^{-2}	35.2
		0.1 M K_2SO_4 (pH 2)	73.5	419.2	195 at 200 mA cm^{-2}	N/A
		0.05 M K_2SO_4 (pH 2)	71.9	358.7	N/A	N/A
Nat. Synth., 2023, **2**, 403–412.	COF:PFSA-modified Cu	3 M K^+ (pH 1)	78	301	30 at 200 mA cm^{-2}	75
Angew. Chem. Int. Ed., 2023, **62**, e202300226.	SiC-Nafion/Cu/PTFE	3 M KCl (pH 1)	45 for C_2H_4	N/A	30 at 100 mA cm^{-2}	N/A
Angew. Chem. Int. Ed., 2023, **62**, e202216102.	GDE Modified Cu/PTFE	0.1 M $KHPO_4$ (pH 2)	55.2	27.61	6 at 50 mA cm^{-2}	N/A
Adv. Funct. Mater., 2025, **35**, 2425636.	Cu/ABSA-PANI	1M KCl (pH 1)	81	700	11 at 600 mA cm^{-2}	52.5
Nat. Nanotechnol., 2024, **19**, 311–318.	CoPc@HC/Cu	0.5 M H_3PO_4 + 0.5 M KH_2PO_4 + 2.5 M KCl	79.6	698	16 at 800 mA cm^{-2}	90
Angew. Chem. Int. Ed., 2025, **65**, e16139	ZNS-Nafion/Cu	0.5 M H_3PO_4 + 0.5 M KH_2PO_4 + 0.5 M K_2SO_4 (pH 2)	80.9	484	10 at 300 mA cm^{-2}	33
Nat. Commun., 2025, **16**, 10727.	YSZ/CuO	3 M KCl (pH 2)	81.6	808	14 at 400 mA cm^{-2}	56.8
ACS Catal., 2025, **15**, 19227–19237	$dCu(OH)_2/Ca_{1/20}$	3 M KCl (pH 2)	81.2	568	10 at 700 mA cm^{-2}	31.2 for EtOH
ACS Catal. 2024, **14**, 8310–8316	Cu-I_2	0.05 M H_2SO_4/0.3 M KI/20 mM I^2	71.02	420	8 at 500 mA cm^{-2}	54
J. Am. Chem. Soc., 2026, **148**, 13444–13453.	$Zr_{1.0\%}$-Cu/BTD	3 M KCl (pH 1.5)	74.9	438	24 at 300 mA cm^{-2}	79.9 for C_{2+}
J. Am. Chem. Soc., 2026, **148**, 7159–7170	PTNs/PCN-Ni/Cu	0.25 M K_2SO_4 (pH 2)	86.2	344.4	227 at 200 mA cm^{-2}	53.4
Nat. Synth., 2025, **4**, 262–270.	Cu-DACs	2.5 M KCl (pH 1)	91	164	10 at 150 mA cm^{-2}	78

Note: Minor deviations may exist due to data extracted from figures.

Reference

1. Y. Xie, P. Ou, X. Wang, Z. Xu, Y. C. Li, Z. Wang, J. E. Huang, J. Wicks, C. McCallum, N. Wang, Y. Wang, T. Chen, B. T. W. Lo, D. Sinton, J. C. Yu, Y. Wang and E. H. Sargent, *Nat. Catal.*, 2022, **5**, 564-570.
2. L.-C. Weng, A. T. Bell and A. Z. Weber, *Energy Environ. Sci.*, 2019, **12**, 1950-1968.
3. S. Gondal, N. Asif, H. F. Svendsen and H. Knuutila, *Chem. Eng. Sci.*, 2015, **123**, 487-499.
4. K. G. Schulz, U. Riebesell, B. Rost, S. Thoms and R. E. Zeebe, *Mar. Chem.*, 2006, **100**, 53-65.
5. G. Kresse and J. Furthmüller, *Comput. Mater. Sci.*, 1996, **6**, 15-50.
6. G. Kresse and J. Furthmüller, *Phys. Rev. B*, 1996, **54**, 11169-11186.
7. P. E. Blochl, *Phys. Rev. B*, 1994, **50**, 17953-17979.
8. J. P. Perdew and Y. Wang, *Phys. Rev. B*, 1992, **46**, 12947-12954.
9. J. P. Perdew, K. Burke and M. Ernzerhof, *Phys. Rev. Lett.*, 1996, **77**, 3865-3868.
10. S. Grimme, J. Antony, S. Ehrlich and H. Krieg, *J. Chem. Phys.*, 2010, **132**, 154104.
11. J. Wu, G. Gao, G. Wu, B. Liu, H. Yang, X. Zhou and J. Wang, *Phys. Chem. Chem. Phys.*, 2014, **16**, 22974-22978.
12. T. D. Kuhne, M. Iannuzzi, M. Del Ben, V. V. Rybkin, P. Seewald, F. Stein, T. Laino, R. Z. Khaliullin, O. Schutt, F. Schiffmann, D. Golze, J. Wilhelm, S. Chulkov, M. H. Bani-Hashemian, V. Weber, U. Borstnik, M. Taillefumier, A. S. Jakobovits, A. Lazzaro, H. Pabst, T. Muller, R. Schade, M. Guidon, S. Andermatt, N. Holmberg, G. K. Schenter, A. Hehn, A. Bussy, F. Belleflamme, G. Tabacchi, A. Gloss, M. Lass, I. Bethune, C. J. Mundy, C. Plessl, M. Watkins, J. VandeVondele, M. Krack and J. Hutter, *J. Chem. Phys.*, 2020, **152**, 194103.
13. S. Goedecker, M. Teter and J. Hutter, *Phys. Rev. B*, 1996, **54**, 1703-1710.
14. C. Hartwigsen, S. Goedecker and J. Hutter, *Phys. Rev. B*, 1998, **58**, 3641-3662.
15. G. Lippert, J. Hutter and M. Parrinello, *Theor. Chem. Acc.*, 1999, **103**, 124-140.
16. J. VandeVondele and J. Hutter, *J. Chem. Phys.*, 2007, **127**.
17. G. Bussi, D. Donadio and M. Parrinello, *J. Chem. Phys.*, 2007, **126**, 014101.
18. T. Lu and F. Chen, *J. Comput. Chem.*, 2012, **33**, 580-592.
19. T. Lu, *J. Chem. Phys.*, 2024, **161**, 082503
20. J. K. Nørskov, J. Rossmeisl, A. Logadottir and L. Lindqvist, *J. Phys. Chem. B*, 2004, **108**, 17886-17892.